

MIT Open Access Articles

Measurement of Resonant and CP Components in $[\bar{B} \rightarrow s] \rightarrow J/\psi n^{+} n^{-}$ Decays

The MIT Faculty has made this article openly available. **Please share** how this access benefits you. Your story matters.

Citation: Aaij, R., B. Adeva, M. Adinolfi, A. Affolder, Z. Ajaltouni, J. Albrecht, F. Alessio, et al. "Measurement of Resonant and CP Components in $[\bar{B} \rightarrow s] \rightarrow J/\psi n^{+} n^{-}$ Decays." Phys. Rev. D 89, no. 9 (May 2014). © 2014 CERN, for the LHCb Collaboration

As Published: <http://dx.doi.org/10.1103/PhysRevD.89.092006>

Publisher: American Physical Society

Persistent URL: <http://hdl.handle.net/1721.1/89022>

Version: Final published version: final published article, as it appeared in a journal, conference proceedings, or other formally published context

Terms of Use: Article is made available in accordance with the publisher's policy and may be subject to US copyright law. Please refer to the publisher's site for terms of use.



Measurement of resonant and CP components in $\bar{B}_s^0 \rightarrow J/\psi \pi^+ \pi^-$ decays

 R. Aaij *et al.**

(LHCb Collaboration)

(Received 25 February 2014; published 14 May 2014)

Structure of the decay $\bar{B}_s^0 \rightarrow J/\psi \pi^+ \pi^-$ is studied using data corresponding to 3 fb^{-1} of integrated luminosity from pp collisions produced by the LHC and collected by the LHCb detector. Five interfering $\pi^+ \pi^-$ states are required to describe the decay: $f_0(980)$, $f_0(1500)$, $f_0(1790)$, $f_2(1270)$, and $f_2'(1525)$. An alternative model including these states and a nonresonant $J/\psi \pi^+ \pi^-$ component also provides a good description of the data. Based on the different transversity components measured for the spin-2 intermediate states, the final state is found to be compatible with being entirely CP odd. The CP -even part is found to be $< 2.3\%$ at a 95% confidence level. The $f_0(500)$ state is not observed, allowing a limit to be set on the absolute value of the mixing angle with the $f_0(980)$ of $< 7.7^\circ$ at a 90% confidence level, consistent with a tetraquark interpretation of the $f_0(980)$ substructure.

DOI: 10.1103/PhysRevD.89.092006

PACS numbers: 14.40.Nd, 13.20.He, 14.40.Be

I. INTRODUCTION

CP violation studies in the $\bar{B}_s^0 \rightarrow J/\psi \pi^+ \pi^-$ decay mode complement studies using $\bar{B}_s^0 \rightarrow J/\psi \phi$ and improve the final accuracy in the measurement of the CP -violating phase, ϕ_s [1]. While the CP content was previously shown to be more than 97.7% CP odd at a 95% confidence level (C.L.), it is important to determine the size of any CP -even components, as these could ultimately affect the uncertainty on the final result for ϕ_s . Since the $\pi^+ \pi^-$ system can form light scalar mesons, such as the $f_0(500)$ and $f_0(980)$, we can investigate if these states have a quark-antiquark or tetraquark structure, and determine the mixing angle between these states [2]. The tree-level Feynman diagram for the process is shown in Fig. 1.

We have previously studied the resonance structure in $\bar{B}_s^0 \rightarrow J/\psi \pi^+ \pi^-$ decays using data corresponding to an integrated luminosity of 1 fb^{-1} [3].¹ In this paper we use 3 fb^{-1} of luminosity, and we also change the analysis technique substantially. Here, the $\pi^+ \pi^-$ mass and all three decay angular distributions are used to determine the resonant and nonresonant components. Previously, the angle between the decay planes of $J/\psi \rightarrow \mu^+ \mu^-$ and $\pi^+ \pi^-$ in the \bar{B}_s^0 rest frame, χ , was integrated over. This simplified the analysis, but sacrificed some precision and also prohibited us from measuring separately the helicity $+1$ and -1 components of any $\pi^+ \pi^-$ resonance, knowledge of which would permit us to evaluate the CP composition of resonances with spin greater than or equal to 1. Since one of the particles in the final state, the J/ψ , has spin 1, its

three decay amplitudes must be considered, while the $\pi^+ \pi^-$ system is described as the coherent sum of resonant and possibly nonresonant amplitudes.

II. AMPLITUDE FORMULA FOR $\bar{B}_s^0 \rightarrow J/\psi h^+ h^-$

The decay of $\bar{B}_s^0 \rightarrow J/\psi h^+ h^-$, where h denotes a pseudoscalar meson, followed by $J/\psi \rightarrow \mu^+ \mu^-$ can be described by four variables. We take the invariant mass of $h^+ h^-$ (m_{hh}) and three helicity angles defined as (i) $\theta_{J/\psi}$, the angle between the μ^+ direction in the J/ψ rest frame with respect to the J/ψ direction in the \bar{B}_s^0 rest frame; (ii) θ_{hh} , the angle between the h^+ direction in the $h^+ h^-$ rest frame with respect to the $h^+ h^-$ direction in the \bar{B}_s^0 rest frame; and (iii) χ , the angle between the J/ψ and $h^+ h^-$ decay planes in the \bar{B}_s^0 rest frame. Figure 2 shows these angles pictorially.² In this paper, hh is equivalent to $\pi^+ \pi^-$.

From the time-dependent decay rate of $\bar{B}_s^0 \rightarrow J/\psi h^+ h^-$ derived in Ref. [4], the time-integrated and flavor-averaged decay rate is proportional to the function

$$S(m_{hh}, \theta_{hh}, \theta_{J/\psi}, \chi) = |A(m_{hh}, \theta_{hh}, \theta_{J/\psi}, \chi)|^2 + |\bar{A}(m_{hh}, \theta_{hh}, \theta_{J/\psi}, \chi)|^2 - 2\text{DRe}\left(\frac{q}{p} A^*(m_{hh}, \theta_{hh}, \theta_{J/\psi}, \chi) \times \bar{A}(m_{hh}, \theta_{hh}, \theta_{J/\psi}, \chi)\right), \quad (1)$$

where \bar{A} , the amplitude of $\bar{B}_s^0 \rightarrow J/\psi h^+ h^-$ at proper time $t = 0$, is a function of m_{hh} , $\theta_{J/\psi}$, θ_{hh} , χ , and is summed over all resonant (and possibly nonresonant) components; q and p are complex parameters that describe the relation between mass and flavor eigenstates [5]. The interference

²These definitions are the same for B_s^0 and \bar{B}_s^0 —namely, μ^+ and h^+ are used to define the angles in both cases.

* Full author list given at the end of the article.

Published by the American Physical Society under the terms of the Creative Commons Attribution 3.0 License. Further distribution of this work must maintain attribution to the author(s) and the published articles title, journal citation, and DOI.

¹Charged conjugated modes are also used when appropriate.

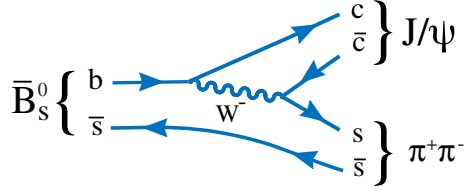


FIG. 1 (color online). Leading-order diagram for \bar{B}_s^0 decays into $J/\psi \pi^+ \pi^-$.

term arises because we must sum the \bar{B}_s^0 and B_s^0 amplitudes before squaring. Even when integrating over proper time, the terms proportional to $\sinh(\Delta\Gamma_s t/2)$ do not vanish because of the finite $\Delta\Gamma_s$ in the B_s^0 system, where $\Delta\Gamma_s$ is the width difference between the light and the heavy mass eigenstates. The factor \mathcal{D} is

$$\mathcal{D} = \frac{\int_0^\infty \varepsilon(t) e^{-\Gamma_s t} \sinh \frac{\Delta\Gamma_s t}{2} dt}{\int_0^\infty \varepsilon(t) e^{-\Gamma_s t} \cosh \frac{\Delta\Gamma_s t}{2} dt}, \quad (2)$$

where Γ_s is the average B_s^0 decay width, and $\varepsilon(t)$ is the detection efficiency as a function of t . For a uniform efficiency, $\mathcal{D} = \Delta\Gamma_s/(2\Gamma_s)$ and is $(6.2 \pm 0.9)\%$ [6].

The amplitude, $A_R(m_{hh})$, is used to describe the mass line shape of the resonance R , that in most cases is a Breit-Wigner function. It is combined with the \bar{B} resonance decay properties to form the expression

$$\mathcal{A}_R(m_{hh}) = \sqrt{2J_R + 1} \sqrt{P_R P_B} F_B^{(L_B)} F_R^{(L_R)} A_R(m_{hh}) \times \left(\frac{P_B}{m_B}\right)^{L_B} \left(\frac{P_R}{m_{hh}}\right)^{L_R}. \quad (3)$$

Here P_B is the J/ψ momentum in the \bar{B}_s^0 rest frame, P_R is the momentum of either of the two hadrons in the dihadron rest frame, m_B is the \bar{B}_s^0 mass, J_R is the spin of R , L_B is the orbital angular momentum between the J/ψ and h^+h^- system, and L_R is the orbital angular momentum in the h^+h^- decay, and thus is the same as the spin of the h^+h^- resonance. $F_B^{(L_B)}$ and $F_R^{(L_R)}$ are the Blatt-Weisskopf barrier factors for the \bar{B}_s^0 and R resonance, respectively [3]. The factor $\sqrt{P_R P_B}$ results from converting the phase space of the natural Dalitz plot variables m_{hh}^2 and $m_{J/\psi h^+}^2$ to that

of m_{hh} and $\cos \theta_{hh}$ [7]. We must sum over all final states, R , so for each J/ψ helicity, denoted by λ , equal to 0, +1, and -1, we have

$$\mathcal{H}_\lambda^{(-)}(m_{hh}, \theta_{hh}) = \sum_R \mathbf{h}_\lambda^R A_R(m_{hh}) d_{-\lambda,0}^{J_R}(\theta_{hh}), \quad (4)$$

where \mathbf{h}_λ^R are the complex coefficients for each helicity amplitude, and the Wigner d functions are listed in Ref. [6].

The decay rates, $|A(m_{hh}, \theta_{hh}, \theta_{J/\psi}, \chi)|^2$, and the interference term, $A^*(m_{hh}, \theta_{hh}, \theta_{J/\psi}, \chi) A(m_{hh}, \theta_{hh}, \theta_{J/\psi}, \chi)$, can be written as functions of $\mathcal{H}_\lambda^{(-)}(m_{hh}, \theta_{hh})$, $\theta_{J/\psi}$, and χ . These relationships are given in Ref. [4]. In order to use the CP relations, it is convenient to replace the helicity complex coefficients \mathbf{h}_λ^R with the complex transversity coefficients \mathbf{a}_τ^R using the relations

$$\begin{aligned} \mathbf{h}_0^R &= \mathbf{a}_0^R, \\ \mathbf{h}_+^R &= \frac{1}{\sqrt{2}} (\mathbf{a}_\parallel^R + \mathbf{a}_\perp^R), \\ \mathbf{h}_-^R &= \frac{1}{\sqrt{2}} (\mathbf{a}_\parallel^R - \mathbf{a}_\perp^R). \end{aligned} \quad (5)$$

Here \mathbf{a}_0^R corresponds to longitudinal polarization of the J/ψ meson, and the other two coefficients correspond to polarizations of the J/ψ meson and h^+h^- system transverse to the decay axis: \mathbf{a}_\parallel^R for parallel polarization of the J/ψ and h^+h^- , and \mathbf{a}_\perp^R for perpendicular polarization.

Assuming no direct CP violation, as this has not been observed in $\bar{B}_s^0 \rightarrow J/\psi \phi$ decays [1], the relation between the \bar{B}_s^0 and B_s^0 variables is $\bar{\mathbf{a}}_\tau^R = \eta_\tau^R \mathbf{a}_\tau^R$, where η_τ^R is the CP eigenvalue of the τ transversity component for the intermediate state R , where τ denotes the 0, \parallel , or \perp component. The final-state CP parities for S, P, and D waves are given in Table I.

In this analysis, a fit determines the amplitude strength a_τ^R and the phase ϕ_τ^R of the amplitude

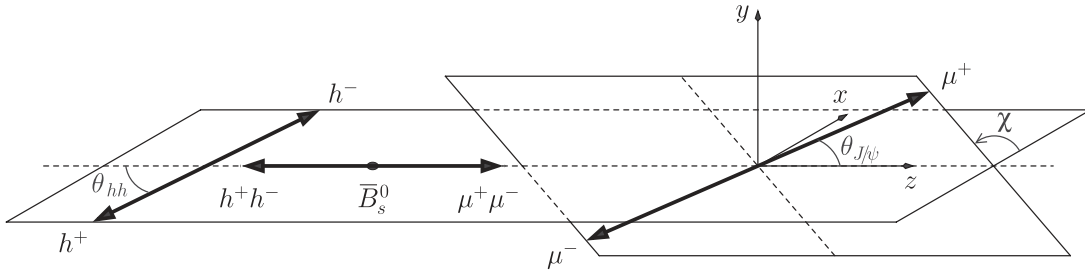


FIG. 2. Definition of helicity angles. For details see text.

TABLE I. CP parity for different spin resonances. Note that spin 0 only has the transversity component 0.

Spin	η_0	η_{\parallel}	η_{\perp}
0	-1
1	1	1	-1
2	-1	-1	1

$$\mathbf{a}_{\tau}^R = a_{\tau}^R e^{i\phi_{\tau}^R} \quad (6)$$

for each resonance R and each transversity τ . For the $\tau = \perp$ amplitude, the L_B value of a spin-1 (or spin-2) resonance is 1 (or 2); the other transversity components have two possible L_B values of 0 and 2 (or 1 and 3) for spin-1 (or spin-2) resonances. In this analysis, the lower one is used. It is verified that our results are insensitive to the L_B choices.

III. DATA SAMPLE AND DETECTOR

The data sample corresponds to an integrated luminosity of 3 fb^{-1} collected with the LHCb detector [8] using pp collisions. One third of the data was acquired at a center-of-mass energy of 7 TeV, and the remainder at 8 TeV. The detector is a single-arm forward spectrometer covering the pseudorapidity range $2 < \eta < 5$, designed for the study of particles containing b or c quarks. The detector includes a high-precision tracking system consisting of a silicon-strip vertex detector surrounding the pp interaction region, a large-area silicon-strip detector located upstream of a dipole magnet with a bending power of about 4 Tm, and three stations of silicon-strip detectors and straw drift tubes [9] placed downstream. The combined tracking system provides a momentum³ measurement with relative uncertainty that varies from 0.4% at 5 GeV to 0.6% at 100 GeV, and an impact parameter (IP) resolution of $20 \text{ } \mu\text{m}$ for tracks with large transverse momentum (p_T). Different types of charged hadrons are distinguished by information from two ring-imaging Cherenkov detectors (RICH) [10]. Photon, electron, and hadron candidates are identified by a calorimeter system consisting of scintillating pad and preshower detectors, an electromagnetic calorimeter, and a hadronic calorimeter. Muons are identified by a system composed of alternating layers of iron and multiwire proportional chambers [11].

The trigger consists of a hardware stage, based on information from the calorimeter and muon systems, followed by a software stage that applies a full event reconstruction [12]. Events selected for this analysis are triggered by a $J/\psi \rightarrow \mu^+\mu^-$ decay, where the J/ψ is required at the software level to be consistent with coming from the decay of a \bar{B}_s^0 meson by the use of either IP requirements or detachment of the J/ψ from the primary

vertex (PV). In the simulation, pp collisions are generated using PYTHIA [13] with a specific LHCb configuration [14]. Decays of hadronic particles are described by EVTGEN [15], in which final-state radiation is generated using PHOTOS [16]. The interaction of the generated particles with the detector and its response are implemented using the GEANT4 toolkit [17] as described in Ref. [18].

IV. EVENT SELECTION

Preselection criteria are implemented to preserve a large fraction of the signal events and are identical to those used in Ref. [19]. A $\bar{B}_s^0 \rightarrow J/\psi \pi^+\pi^-$ candidate is reconstructed by combining a $J/\psi \rightarrow \mu^+\mu^-$ candidate with two pions of opposite charge. To ensure good track reconstruction, each of the four particles in the \bar{B}_s^0 candidate is required to have the track fit $\chi^2/\text{n.d.f.}$ to be less than 4, where n.d.f. is the number of degrees of freedom of the fit. The $J/\psi \rightarrow \mu^+\mu^-$ candidate is formed by two identified muons of opposite charge having p_T greater than 500 MeV, and with a geometrical fit vertex χ^2 less than 16. Only candidates with a dimuon invariant mass between -48 MeV and $+43 \text{ MeV}$ from the observed J/ψ mass peak are selected, and they are then constrained to the J/ψ mass [6] for subsequent use.

Pion candidates are required to each have a p_T greater than 250 MeV, and the sum, $p_T(\pi^+) + p_T(\pi^-)$, must be larger than 900 MeV. Both pions must have χ_{IP}^2 greater than 9 to reject particles produced from the PV. (The reconstruction procedure and the PV resolution are given in Ref. [20].) The χ_{IP}^2 is computed as the difference between the χ^2 's of the PV reconstructed with and without the considered track. Both pions must also come from a common vertex with $\chi^2/\text{n.d.f.} < 16$ and form a vertex with the J/ψ with a $\chi^2/\text{n.d.f.}$ less than 10 (here n.d.f. equals 5). Pion candidates are identified using the RICH and muon systems. The particle identification makes use of the logarithm of the likelihood ratio comparing two particle hypotheses (DLL). For pion selection, we require $\text{DLL}(\pi - K) > -10$ and $\text{DLL}(\pi - \mu) > -10$.

The \bar{B}_s^0 candidate must have a flight distance of more than 1.5 mm. The angle between the combined momentum vector of the decay products and the vector formed from the positions of the PV and the decay vertex (pointing angle) is required to be less than 2.5° .

Events satisfying this preselection are then further filtered using a multivariate analyzer based on a boosted decision tree (BDT) technique [21]. The BDT uses eight variables that are chosen to provide separation between signal and background. These are the minimum of DLL ($\mu - \pi$) of the μ^+ and μ^- , $p_T(\pi^+) + p_T(\pi^-)$, the minimum of χ_{IP}^2 of the π^+ and π^- , and the \bar{B}_s^0 properties of vertex χ^2 , pointing angle, flight distance, p_T , and χ_{IP}^2 . The BDT is trained on a simulated sample of $\bar{B}_s^0 \rightarrow J/\psi \pi^+\pi^-$ signal events and a background data sample from the sideband

³We work in units where $c = 1$.

$5566 < m(J/\psi\pi^+\pi^-) < 5616$ MeV. Then the BDT is tested on independent samples. The distributions of the BDT classifier for signal and background samples are shown in Fig. 3. By maximizing the signal significance, we set the requirement that the classifier be greater than zero, which has a signal efficiency of 95% and rejects 90% of the background.

The invariant mass of the selected $J/\psi\pi^+\pi^-$ combinations is shown in Fig. 4. There is a large peak at the \bar{B}_s^0 mass and a smaller one at the \bar{B}^0 mass on top of a background.

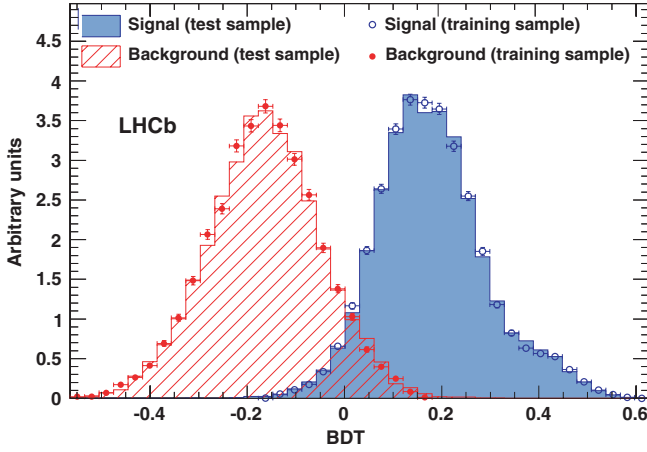


FIG. 3 (color online). Distributions of the BDT classifier for both training and test samples of $J/\psi\pi^+\pi^-$ signal and background events. The signal samples are from simulation, and the background samples are from data.

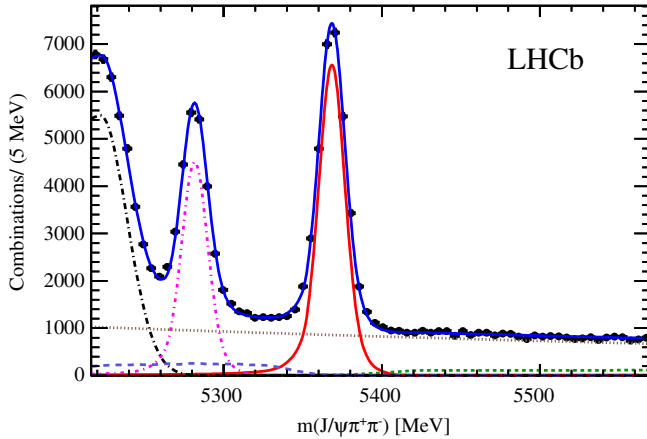


FIG. 4 (color online). Invariant mass of $J/\psi\pi^+\pi^-$ combinations. The data have been fitted with a double Crystal Ball signal and several background functions. The (red) solid curve shows the \bar{B}_s^0 signal, the (brown) dotted line shows the combinatorial background, the (green) short-dashed line shows the B^- background, the (purple) dot-dashed curve is $\bar{B}^0 \rightarrow J/\psi\pi^+\pi^-$, the (light blue) long-dashed line is the sum of $\bar{B}_s^0 \rightarrow J/\psi\eta'$, $\bar{B}_s^0 \rightarrow J/\psi\phi$ with $\phi \rightarrow \pi^+\pi^-\pi^0$ backgrounds and the $\Lambda_b^0 \rightarrow J/\psi K^- p$ reflection, the (black) dot-long dashed curve is the $\bar{B}^0 \rightarrow J/\psi K^- \pi^+$ reflection, and the (blue) solid curve is the total.

A double Crystal Ball function with common means models the radiative tails and is used to fit each of the signals. The known $\bar{B}_s^0 - \bar{B}^0$ mass difference [6] is used to constrain the difference in mean values. Other components in the fit model take into account contributions from $B^- \rightarrow J/\psi K^-(\pi^-)$, $\bar{B}_s^0 \rightarrow J/\psi\eta'$ with $\eta' \rightarrow \rho^0\gamma$, $\bar{B}_s^0 \rightarrow J/\psi\phi$ with $\phi \rightarrow \pi^+\pi^-\pi^0$ backgrounds, and $\bar{B}^0 \rightarrow J/\psi K^- \pi^+$ and $\Lambda_b^0 \rightarrow J/\psi K^- p$ reflections, where the K^- in the former, and both K^- and p in the latter, are misidentified as pions. The shape of the $\bar{B}^0 \rightarrow J/\psi\pi^+\pi^-$ signal is taken to be the same as that of the \bar{B}_s^0 . The combinatorial background shape is taken from like-sign combinations that are the sum of $\pi^+\pi^+$ and $\pi^-\pi^-$ candidates, and it was found to be well described by an exponential function in previous studies [3,22]. The shapes of the other components are taken from simulation with their yields allowed to vary. The $\Lambda_b^0 \rightarrow J/\psi K^- p$ reflection yield in the fit region is constrained to the expected number 2145 ± 201 , which is obtained from study of the events in the control region of $5066 < m(J/\psi\pi^+\pi^-) < 5141$ MeV. The mass fit gives 27396 ± 207 signal and 7075 ± 101 background candidates, leading to the signal fraction $f_{\text{sig}} = (79.5 \pm 0.2)\%$, within ± 20 MeV of the \bar{B}_s^0 mass peak. The effective rms mass resolution is 9.9 MeV.

V. PROBABILITY DENSITY FUNCTION CONSTRUCTION

The correlated distributions of four variables m_{hh} , $\cos\theta_{hh}$, $\cos\theta_{J/\psi}$, and χ are fitted using the candidates within ± 20 MeV of the \bar{B}_s^0 mass peak. To improve the resolution of these variables, we perform a kinematic fit constraining the \bar{B}_s^0 and J/ψ masses to their world average mass values [6] and recompute the final-state momenta.

The overall PDF given by the sum of signal, S , and background functions is

$$F(m_{hh}, \theta_{hh}, \theta_{J/\psi}, \chi) = \frac{f_{\text{sig}}}{\mathcal{N}_{\text{sig}}} \varepsilon(m_{hh}, \theta_{hh}, \theta_{J/\psi}, \chi) \times S(m_{hh}, \theta_{hh}, \theta_{J/\psi}, \chi) + (1 - f_{\text{sig}}) B(m_{hh}, \theta_{hh}, \theta_{J/\psi}, \chi), \quad (7)$$

where ε is the detection efficiency, and B is the background PDF discussed later in Sec. V C. The normalization factor for the signal is given by

$$\mathcal{N}_{\text{sig}} = \int \varepsilon(m_{hh}, \theta_{hh}, \theta_{J/\psi}, \chi) S(m_{hh}, \theta_{hh}, \theta_{J/\psi}, \chi) \times dm_{hh} d\cos\theta_{hh} d\cos\theta_{J/\psi} d\chi. \quad (8)$$

The signal function S is defined in Eq. (1), where $\mathcal{D} = (8.7 \pm 1.5)\%$, taking into account the acceptance [23], and choosing a phase convention $q/p = e^{-i\phi_s}$. The phase ϕ_s is fixed to the standard model value of -0.04

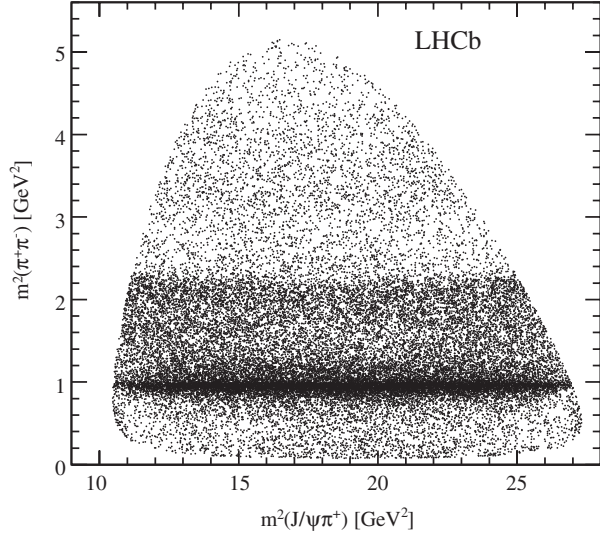


FIG. 5. Distribution of $m^2(\pi^+\pi^-)$ versus $m^2(J/\psi\pi^+)$ for all events within ± 20 MeV of the \bar{B}_s^0 mass peak.

radians [24]. Our results are found to be insensitive to the value of ϕ_s used within the 95% C.L. limits set by the LHCb measurement [1].

A. Data distributions of the Dalitz plot

The event distribution for $m^2(\pi^+\pi^-)$ versus $m^2(J/\psi\pi^+)$ in Fig. 5 shows clear structures in $m^2(\pi^+\pi^-)$. The presence of possible exotic structures in the $J/\psi\pi^+$ system, as claimed in similar decays [25,26], is investigated by examining the $J/\psi\pi^+$ mass distribution shown in Fig. 6(a). No resonant effects are evident. Figure 6(b) shows the $\pi^+\pi^-$ mass distribution. Apart from a large signal peak due to the $f_0(980)$, there are visible structures at about 1450 MeV and 1800 MeV.

B. Detection efficiency

The detection efficiency is determined from a phase-space simulation sample containing 4×10^6 $\bar{B}_s^0 \rightarrow J/\psi\pi^+\pi^-$

events with $J/\psi \rightarrow \mu^+\mu^-$. The efficiency can be parametrized in terms of analysis variables as

$$\varepsilon(m_{hh}, \theta_{hh}, \theta_{J/\psi}, \chi) = \varepsilon_1(s_{12}, s_{13}) \times \varepsilon_2(m_{hh}, \theta_{J/\psi}) \times \varepsilon_3(m_{hh}, \chi), \quad (9)$$

where $s_{12} \equiv m^2(J/\psi\pi^+)$ and $s_{13} \equiv m^2(J/\psi\pi^-)$ are functions of (m_{hh}, θ_{hh}) ; such parameter transformations in ε_1 are implemented in order to use the Dalitz-plot-based efficiency model developed in previous publications [3,19]. The efficiency functions take into account correlations between m_{hh} and each of the three angles as determined by the simulation.

The efficiency as a function of the angle χ is shown in Fig. 7. To simplify the normalization of the PDF, the efficiency as a function of χ is parametrized in 26 bins of m_{hh}^2 as

$$\varepsilon_3(m_{hh}, \chi) = \frac{1}{2\pi} (1 + p_1 \cos \chi + p_2 \cos 2\chi), \quad (10)$$

where $p_1 = p_1^0 + p_1^1 m_{hh}^2$ and $p_2 = p_2^0 + p_2^1 m_{hh}^2 + p_2^2 m_{hh}^4$. A fit to the simulation determines $p_1^0 = 0.0087 \pm 0.0051$, $p_1^1 = (-0.0062 \pm 0.0019) \text{ GeV}^{-2}$, $p_2^0 = 0.0030 \pm 0.0077$, $p_2^1 = (0.053 \pm 0.007) \text{ GeV}^{-2}$, and $p_2^2 = (-0.0077 \pm 0.0015) \text{ GeV}^{-4}$.

The efficiency in $\cos \theta_{J/\psi}$ also depends on m_{hh} ; we fit the $\cos \theta_{J/\psi}$ distributions of the $J/\psi\pi^+\pi^-$ simulation sample with the function

$$\varepsilon_2(m_{hh}, \theta_{J/\psi}) = \frac{1 + a(m_{hh}^2) \cos^2 \theta_{J/\psi}}{2 + 2a(m_{hh}^2)/3}, \quad (11)$$

giving 26 values of a as a function of m_{hh}^2 . The resulting distribution in a is shown in Fig. 8 and is best described by a second-order polynomial function

$$a(m_{hh}^2) = a_0 + a_1 m_{hh}^2 + a_2 m_{hh}^4, \quad (12)$$

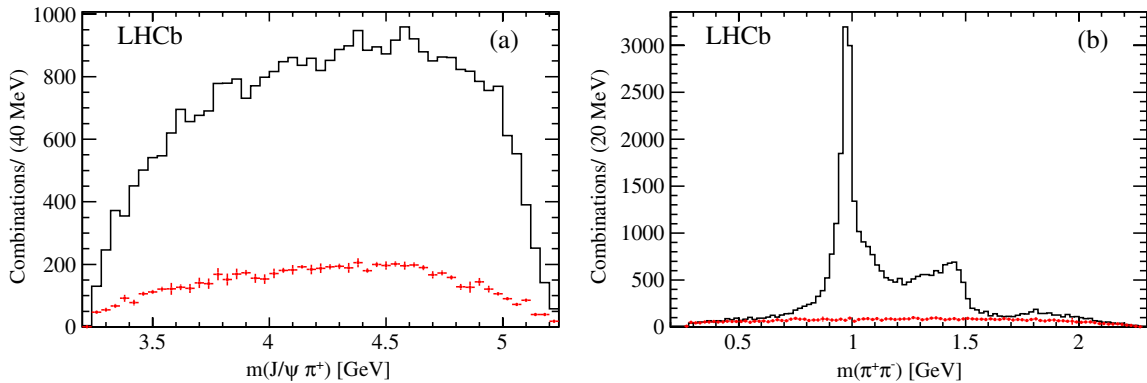


FIG. 6 (color online). Distributions of (a) $m(J/\psi\pi^+)$ and (b) $m(\pi^+\pi^-)$ for $\bar{B}_s^0 \rightarrow J/\psi\pi^+\pi^-$ candidate decays within ± 20 MeV of the \bar{B}_s^0 mass. The (red) points with error bars show the background contribution determined from $m(J/\psi\pi^+\pi^-)$ fits performed in each bin of the plotted variables.

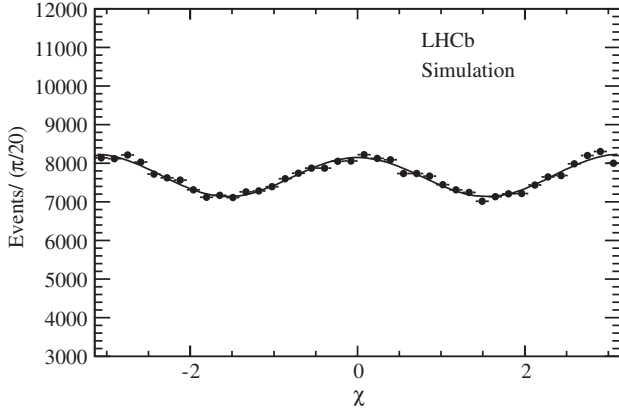


FIG. 7. Distribution of the angle χ for the $J/\psi\pi^+\pi^-$ simulation sample fitted with Eq. (10), used to determine the efficiency parameters.

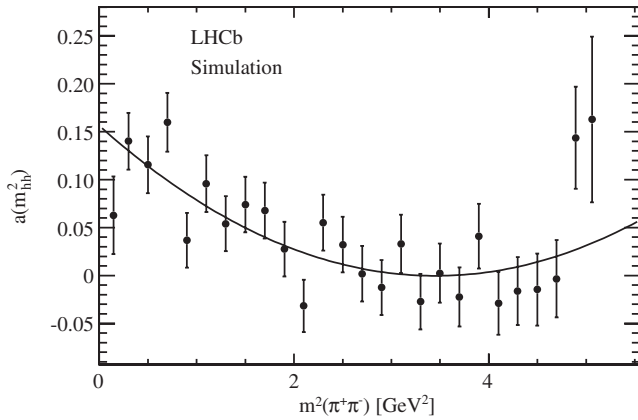


FIG. 8. Second-order polynomial fit to the acceptance parameter $a(m_{hh}^2)$ used in Eq. (11).

with $a_0 = 0.156 \pm 0.020$, $a_1 = (-0.091 \pm 0.018) \text{ GeV}^{-2}$, and $a_2 = (0.013 \pm 0.004) \text{ GeV}^{-4}$.

The function $\epsilon_1(s_{12}, s_{13})$ can be determined from the simulation after integrating over $\cos\theta_{J/\psi}$ and χ , because the functions ϵ_2 and ϵ_3 are normalized in $\cos\theta_{J/\psi}$ and χ ,

respectively. It is parametrized as a symmetric fifth-order polynomial function given by

$$\begin{aligned} \epsilon_1(s_{12}, s_{13}) = & 1 + \epsilon_1(x + y) + \epsilon_2(x + y)^2 + \epsilon_3xy \\ & + \epsilon_4(x + y)^3 + \epsilon_5xy(x + y) + \epsilon_6(x + y)^4 \\ & + \epsilon_7xy(x + y)^2 + \epsilon_8x^2y^2 + \epsilon_9(x + y)^5 \\ & + \epsilon_{10}xy(x + y)^3 + \epsilon_{11}x^2y^2(x + y), \end{aligned} \quad (13)$$

where $x = s_{12}/\text{GeV}^2 - 18.9$, and $y = s_{13}/\text{GeV}^2 - 18.9$. The phase-space simulation is generated uniformly in the two-dimensional distribution of (s_{12}, s_{13}) ; therefore, the distribution of selected events reflects the efficiency and is fit to determine the efficiency parameters ϵ_i . The projections of the fit are shown in Fig. 9, giving the efficiency as a function of $\cos\theta_{\pi^+\pi^-}$ versus $m(\pi^+\pi^-)$ in Fig. 10.

C. Background composition

The main background source is combinatorial and is taken from the like-sign combinations within $\pm 20 \text{ MeV}$ of the \bar{B}_s^0 mass peak. The like-sign combinations also contain the B^- background, which is peaked at $\cos\theta_{hh} = \pm 1$. The like-sign combinations cannot contain any ρ^0 , which is measured to be 3.5% of the total background. To obtain the ρ^0 contribution, the background $m(\pi^+\pi^-)$ distribution shown in Fig. 6(b), found by fitting the $m(J/\psi\pi^+\pi^-)$ distribution in bins of $m(\pi^+\pi^-)$, is compared to the $m(\pi^\pm\pi^\pm)$ distribution from the like-sign combinations. In this way, simulated ρ^0 background is added into the like-sign candidates. The background PDF B is the sum of functions for B^- (B_{B^-}) and for the other (B_{other}), given by

$$\begin{aligned} B(m_{hh}, \theta_{hh}, \theta_{J/\psi}, \chi) = & \frac{1 - f_{B^-}}{\mathcal{N}_{\text{other}}} B_{\text{other}}(m_{hh}, \theta_{hh}, \theta_{J/\psi}, \chi) \\ & + \frac{f_{B^-}}{\mathcal{N}_{B^-}} B_{B^-}(m_{hh}, \theta_{hh}, \theta_{J/\psi}, \chi), \end{aligned} \quad (14)$$

where $\mathcal{N}_{\text{other}}$ and \mathcal{N}_{B^-} are normalization factors, and f_{B^-} is the fraction of the B^- background in the total background. The $J/\psi\pi^+\pi^-$ mass fit gives $f_{B^-} = (1.7 \pm 0.2)\%$.

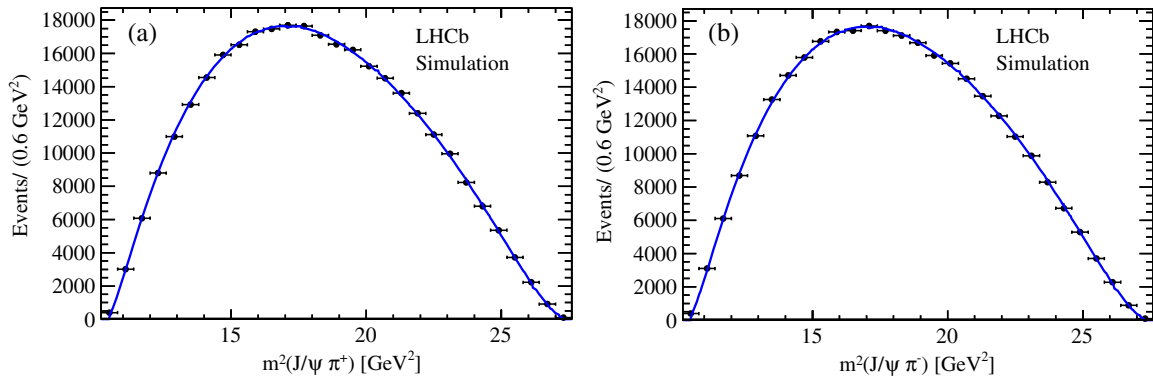


FIG. 9 (color online). Projections of invariant mass squared of (a) $m^2(J/\psi\pi^+)$ and (b) $m^2(J/\psi\pi^-)$ of the simulated Dalitz plot used to measure the efficiency parameters. The points represent the simulated event distributions, and the curves the polynomial fit.

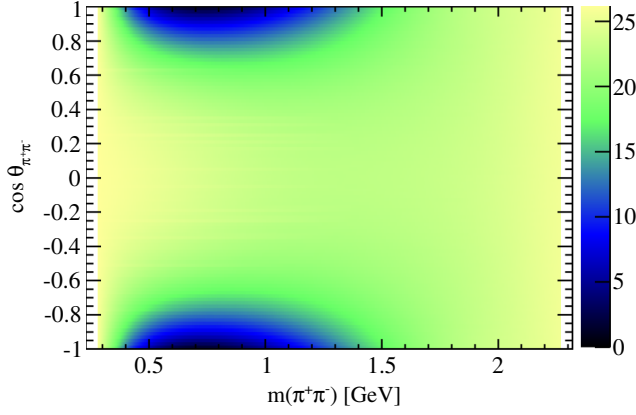


FIG. 10 (color online). Parametrization of the detection efficiency as a function of $\cos \theta_{\pi^+\pi^-}$ and $m(\pi^+\pi^-)$. The scale is arbitrary.

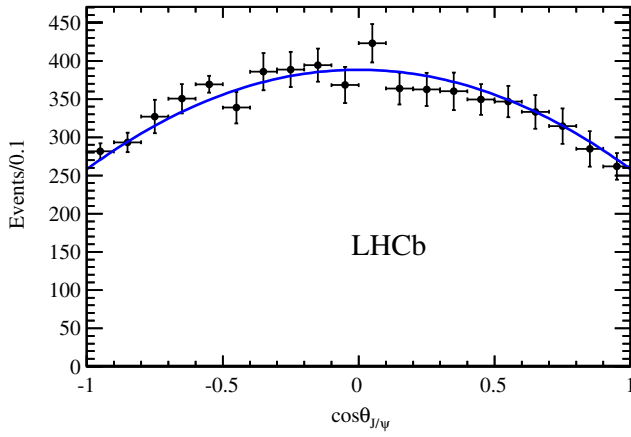
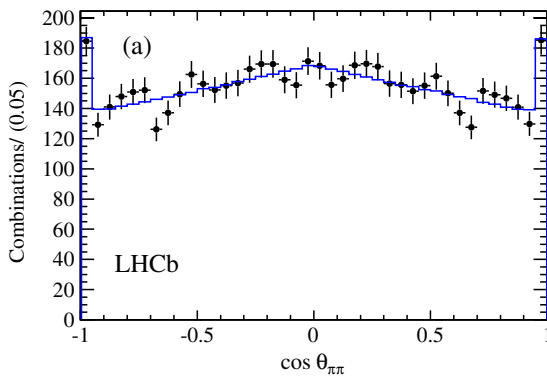


FIG. 11 (color online). Distribution of $\cos \theta_{J/\psi}$ of the other background and the fitted function $1 + \alpha \cos^2 \theta_{J/\psi}$. The points with error bars show the background obtained from candidate mass fits in bins of $\cos \theta_{J/\psi}$.

The B^- background is separated because its invariant mass is very close to the highest allowed limit, resulting in its $\cos \theta_{hh}$ distribution peaking at ± 1 . The function for the B^- background is defined as



$$B_{B^-}(m_{hh}, \theta_{hh}, \theta_{J/\psi}, \chi) = G(m_{hh}; m_0, \sigma_m) \times G(|\cos \theta_{hh}|; 1, \sigma_\theta) \times (1 - \cos^2 \theta_{J/\psi}) \times (1 + p_{b1} \cos \chi + p_{b2} \cos 2\chi), \quad (15)$$

where G is the Gaussian function, and the parameters m_0 , σ_m , σ_θ , p_{b1} , and p_{b2} are determined by the fit. The last term is the same function for χ .

The function for the other background is

$$B_{\text{other}}(m_{hh}, \theta_{hh}, \theta_{J/\psi}, \chi) = m_{hh} B_1(m_{hh}^2, \cos \theta_{hh}) \times (1 + \alpha \cos^2 \theta_{J/\psi}) \times (1 + p_{b1} \cos \chi + p_{b2} \cos 2\chi), \quad (16)$$

where the function

$$B_1(m_{hh}^2, \cos \theta_{hh}) = B_2(\zeta) \frac{p_B}{m_B} \times \frac{1 + c_1 q(\zeta) |\cos \theta_{hh}| + c_2 p(\zeta) \cos^2 \theta_{hh}}{2[1 + c_1 q(\zeta)/2 + c_2 p(\zeta)/3]}. \quad (17)$$

Here $\zeta \equiv 2(m_{hh}^2 - m_{\min}^2)/(m_{\max}^2 - m_{\min}^2) - 1$, where m_{\min} and m_{\max} give the fit boundaries of m_{hh} ; $B_2(\zeta)$ is a fifth-order Chebychev polynomial; and $q(\zeta)$ and $p(\zeta)$ are both second-order Chebychev polynomials with the coefficients c_1 and c_2 being free parameters. In order to better approximate the real background in the \bar{B}_s^0 signal region, the $J/\psi \pi^\pm \pi^\pm$ candidates are kinematically constrained to the \bar{B}_s^0 mass, and $\mu^+ \mu^-$ to the J/ψ mass.

The second part $(1 + \alpha \cos^2 \theta_{J/\psi})$ is a function of the J/ψ helicity angle. The $\cos \theta_{J/\psi}$ distribution of the background is shown in Fig. 11; fitting with the function determines the parameter $\alpha = -0.34 \pm 0.03$. A fit to the like-sign combinations added with additional ρ^0 background determines the parameters describing the m_{hh} , θ_{hh} , and χ distributions.

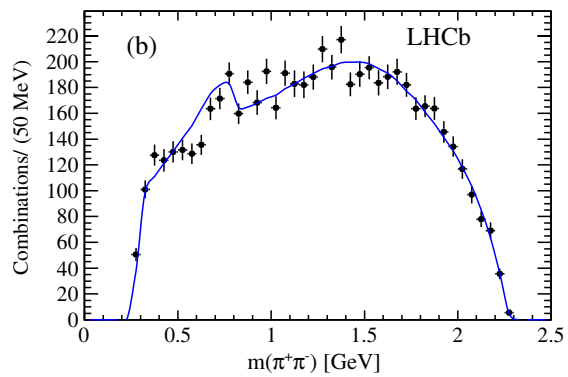


FIG. 12 (color online). Projections of (a) $\cos \theta_{\pi\pi}$ and (b) $m(\pi^+\pi^-)$ of the total background. The (blue) histogram or curve is a projection of the fit, and the points with error bars show the like-sign combinations added with additional ρ^0 background.

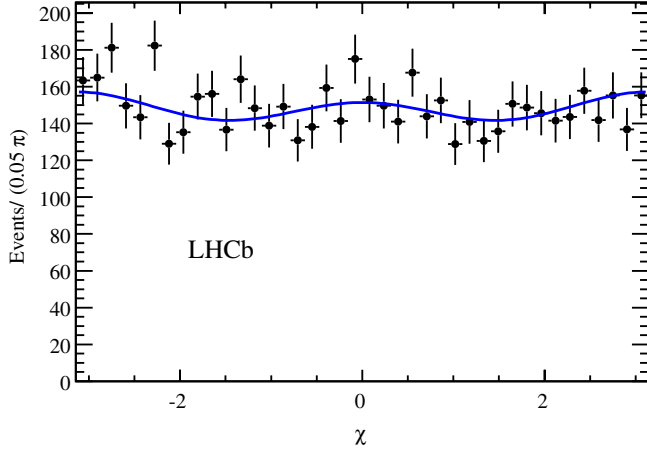


FIG. 13 (color online). Distribution of χ of the total background and the fitted function. The points with error bars show the like-sign combinations added with additional ρ^0 background.

Figures 12 and 13 show the projections of $\cos\theta_{hh}$ and m_{hh} , and of χ of the total background, respectively.

VI. FINAL-STATE COMPOSITION

A. Resonance models

To study the resonant structures of the decay $\bar{B}_s^0 \rightarrow J/\psi\pi^+\pi^-$, we use the 34 471 candidates with invariant mass lying within ± 20 MeV of the \bar{B}_s^0 mass peak, which include 7075 ± 101 background events. The $\pi^+\pi^-$ resonance candidates that could contribute to $\bar{B}_s^0 \rightarrow J/\psi\pi^+\pi^-$ decay are listed in Table II. The resonances that decay into a $\pi^+\pi^-$ pair must be isoscalar ($I = 0$), because the $s\bar{s}$ system forming the resonances in Fig. 1 has $I = 0$. To test the isoscalar argument, the isospin-1 $\rho(770)$ meson is also added to the baseline fit. The nonresonance (NR) is assumed to be S wave, its shape is defined by Eq. (3) where the amplitude function $A_R(m_{hh})$ is set to be equal to 1, and the Blatt-Weisskopf barrier factors $F_B^{(1)}$ and $F_R^{(0)}$ are both set to 1.

In the previous analysis [23], we observed a resonant state at (1475 ± 6) MeV with a width of (113 ± 11) MeV. We identified it with the $f_0(1370)$, though its mass and

width values agreed neither with the $f_0(1500)$ nor with the $f_0(1370)$. W. Ochs [29] argues that the better assignment is $f_0(1500)$; we follow his suggestion. In addition, a structure is clearly visible in the 1800 MeV region [see Fig. 6(b)], which was not the case in our previous analysis [3]. This could be the $f_0(1790)$ resonance observed by BES [28] in $J/\psi \rightarrow \phi\pi^+\pi^-$ decays.

From the measured ratios $\mathcal{B}(\bar{B}_s^0 \rightarrow J/\psi f_2'(1525))/\mathcal{B}(\bar{B}_s^0 \rightarrow J/\psi\phi)$ [27] and $\mathcal{B}(\bar{B}_s^0 \rightarrow J/\psi\pi^+\pi^-)/\mathcal{B}(\bar{B}_s^0 \rightarrow J/\psi\phi)$ [3], using the measured $\pi^+\pi^-$ and K^+K^- branching fractions [6], the expected $f_2'(1525)$ fit fraction for the transversity-0 component is $(0.45 \pm 0.13)\%$, and the ratio of helicity $\lambda = 0$ to $|\lambda| = 1$ components, which is equal to the ratio of transversity-0 to the sum of \perp and \parallel components, is 1.9 ± 0.8 , where the uncertainties are dominated by that on $f_2'(1525)$ fit fractions in $\bar{B}_s^0 \rightarrow J/\psi K^+K^-$ decays. This information is used as constraints in the fit.

The masses and widths of the resonances are also listed in Table II. When used in the fit, they are fixed to these central values, except for the parameters of $f_0(980)$ and $f_0(1500)$ that are determined by the fit. In addition, the parameters of $f_0(1790)$ are constrained to those determined by the BES measurement [28].

As suggested by D. V. Bugg [30], the Flatté model [31] for $f_0(980)$ is slightly modified and is parametrized as

$$A_R(m_{\pi^+\pi^-}) = \frac{1}{m_R^2 - m_{\pi^+\pi^-}^2 - im_R(g_{\pi\pi}\rho_{\pi\pi} + g_{KK}F_{KK}^2\rho_{KK})}, \quad (18)$$

where m_R is the $f_0(980)$ pole mass, the parameters $g_{\pi\pi}$ and g_{KK} are the $f_0(980)$ coupling constants to the $\pi^+\pi^-$ and K^+K^- final states, respectively, and the phase-space ρ factors are given by Lorentz-invariant phase spaces as

$$\rho_{\pi\pi} = \frac{2}{3} \sqrt{1 - \frac{4m_{\pi^\pm}^2}{m_{\pi^+\pi^-}^2}} + \frac{1}{3} \sqrt{1 - \frac{4m_{\pi^0}^2}{m_{\pi^+\pi^-}^2}}, \quad (19)$$

$$\rho_{KK} = \frac{1}{2} \sqrt{1 - \frac{4m_{K^\pm}^2}{m_{\pi^+\pi^-}^2}} + \frac{1}{2} \sqrt{1 - \frac{4m_{K^0}^2}{m_{\pi^+\pi^-}^2}}. \quad (20)$$

TABLE II. Possible resonance candidates in the $\bar{B}_s^0 \rightarrow J/\psi\pi^+\pi^-$ decay mode and their parameters used in the fit.

Resonance	Spin	Helicity	Resonance formalism	Mass (MeV)	Width (MeV)	Source
$f_0(500)$	0	0	BW	471 ± 21	534 ± 53	LHCb [19]
$f_0(980)$	0	0	Flatté		See text	
$f_2(1270)$	2	0, ± 1	BW	1275.1 ± 1.2	$185.1^{+2.9}_{-2.4}$	PDG [6]
$f_0(1500)$	0	0	BW		See text	
$f_2'(1525)$	2	0, ± 1	BW	1522^{+6}_{-3}	84^{+12}_{-8}	LHCb [27]
$f_0(1710)$	0	0	BW	1720 ± 6	135 ± 8	PDG [6]
$f_0(1790)$	0	0	BW	1790^{+40}_{-30}	270^{+60}_{-30}	BES [28]
$\rho(770)$	1	0, ± 1	BW	775.49 ± 0.34	149.1 ± 0.8	PDG [6]

TABLE III. Fit $-\ln \mathcal{L}$ and $\chi^2/\text{n.d.f.}$ of different resonance models.

Resonance model	$-\ln \mathcal{L}$	$\chi^2/\text{n.d.f.}$
5R (Solution I)	-93738	2005/1822 = 1.100
5R + NR (Solution I)	-93741	2003/1820 = 1.101
5R + $f_0(500)$ (Solution I)	-93741	2004/1820 = 1.101
5R + $f_0(1710)$ (Solution I)	-93744	1998/1820 = 1.098
5R + $\rho(770)$ (Solution I)	-93742	2004/1816 = 1.104
5R + NR (Solution II)	-93739	2008/1820 = 1.103
5R + NR + $f_0(500)$ (Solution II)	-93741	2004/1818 = 1.102
5R + NR + $f_0(1710)$ (Solution II)	-93745	2004/1818 = 1.102
5R + NR + $\rho(770)$ (Solution II)	-93746	1998/1814 = 1.101

TABLE IV. Fit fractions (%) of contributing components for both solutions.

Component	Solution I	Solution II
$f_0(980)$	$70.3 \pm 1.5^{+0.4}_{-5.1}$	$92.4 \pm 2.0^{+0.8}_{-16.0}$
$f_0(1500)$	$10.1 \pm 0.8^{+1.1}_{-0.3}$	$9.1 \pm 0.9 \pm 0.3$
$f_0(1790)$	$2.4 \pm 0.4^{+5.0}_{-0.2}$	$0.9 \pm 0.3^{+2.5}_{-0.1}$
$f_2(1270)_0$	$0.36 \pm 0.07 \pm 0.03$	$0.42 \pm 0.07 \pm 0.04$
$f_2(1270)_\parallel$	$0.52 \pm 0.15^{+0.05}_{-0.02}$	$0.42 \pm 0.13^{+0.11}_{-0.02}$
$f_2(1270)_\perp$	$0.63 \pm 0.34^{+0.16}_{-0.08}$	$0.60 \pm 0.36^{+0.12}_{-0.09}$
$f'_2(1525)_0$	$0.51 \pm 0.09^{+0.05}_{-0.04}$	$0.52 \pm 0.09^{+0.05}_{-0.04}$
$f'_2(1525)_\parallel$	$0.06^{+0.13}_{-0.04} \pm 0.01$	$0.11^{+0.16+0.03}_{-0.07-0.04}$
$f'_2(1525)_\perp$	$0.26 \pm 0.18^{+0.06}_{-0.04}$	$0.26 \pm 0.22^{+0.06}_{-0.05}$
NR	...	$5.9 \pm 1.4^{+0.7}_{-4.6}$
Sum	85.2	110.6
$-\ln \mathcal{L}$	-93738	-93739
$\chi^2/\text{n.d.f.}$	2005/1822	2008/1820

Compared to the normal Flatté function, a form factor $F_{KK} = \exp(-\alpha k^2)$ is introduced above the KK threshold and serves to reduce the ρ_{KK} factor as $m_{\pi^+\pi^-}$ increases, where k is momentum of each kaon in the $\bar{K}K$ rest frame, and $\alpha = (2.0 \pm 0.25) \text{ GeV}^{-2}$ [30]. This parametrization

slightly decreases the $f_0(980)$ width above the KK threshold. The parameter α is fixed to 2.0 GeV^{-2} , as it is not very sensitive to the fit.

To determine the complex amplitudes in a specific model, the data are fitted maximizing the unbinned likelihood, given as

$$\mathcal{L} = \prod_{i=1}^N F(m_{hh}^i, \theta_{hh}^i, \theta_{J/\psi}^i, \chi^i), \quad (21)$$

where N is the total number of candidates, and F is the total PDF defined in Eq. (7). In order to converge properly in a maximum-likelihood method, the PDFs of the signal and background need to be normalized. This is accomplished by first normalizing the χ - and $\cos \theta_{J/\psi}$ -dependent parts analytically, and then normalizing the m_{hh} - and $\cos \theta_{hh}$ -dependent parts using a numerical integration over 1000×200 bins.

The fit determines amplitude magnitudes $a_i^{R_i}$ and phases $\phi_i^{R_i}$ defined in Eq. (6). The $a_0^{f_0(980)}$ amplitude is fixed to 1, since the overall normalization is related to the signal yield. As only relative phases are physically meaningful, $\phi_0^{f_0(980)}$ is fixed to 0. In addition, due to the averaging of B_s^0 and \bar{B}_s^0 , the interference terms between opposite CP states are canceled out, making it not possible to measure the relative phase between CP -even and CP -odd states here, so one CP -even phase, $\phi_\perp^{f_2(1270)}$, is also fixed to 0.

B. Fit fraction

Knowledge of the contribution of each component can be expressed by defining a fit fraction for each transversity τ , \mathcal{F}_τ^R , which is the squared amplitude of R integrated over the phase space divided by the entire amplitude squared over the same area. To determine \mathcal{F}_τ^R , one needs to integrate over all the four fitted observables in the analysis. The interference terms between different helicity components vanish after integrating over the two variables of $\cos \theta_{J/\psi}$ and χ . Thus, we define the transversity fit fraction as

$$\mathcal{F}_\tau^R = \frac{\int |a_\tau^R e^{i\phi_\tau^R} \mathcal{A}_R(m_{hh}) d_{\lambda,0}^{J_R}(\theta_{hh})|^2 dm_{hh} d\cos \theta_{hh}}{\int (|\mathcal{H}_0(m_{hh}, \theta_{hh})|^2 + |\mathcal{H}_+(m_{hh}, \theta_{hh})|^2 + |\mathcal{H}_-(m_{hh}, \theta_{hh})|^2) dm_{hh} d\cos \theta_{hh}}, \quad (22)$$

where $\lambda = 0$ in the d function for $\tau = 0$, and $\lambda = 1$ for $\tau = \perp$ or \parallel .

Note that the sum of the fit fractions is not necessarily unity due to the potential presence of interference between two resonances. Interference term fractions are given by

$$\mathcal{F}_\tau^{RR'} = 2\mathcal{R}e \left(\frac{\int a_\tau^R a_{\tau'}^{R'} e^{i(\phi_\tau^R - \phi_{\tau'}^{R'})} \mathcal{A}_R(m_{hh}) \mathcal{A}_{R'}^*(m_{hh}) d_{\lambda,0}^{J_R}(\theta_{hh}) d_{\lambda',0}^{J_{R'}}(\theta_{hh}) dm_{hh} d\cos \theta_{hh}}{\int (|\mathcal{H}_0(m_{hh}, \theta_{hh})|^2 + |\mathcal{H}_+(m_{hh}, \theta_{hh})|^2 + |\mathcal{H}_-(m_{hh}, \theta_{hh})|^2) dm_{hh} d\cos \theta_{hh}} \right) \quad (23)$$

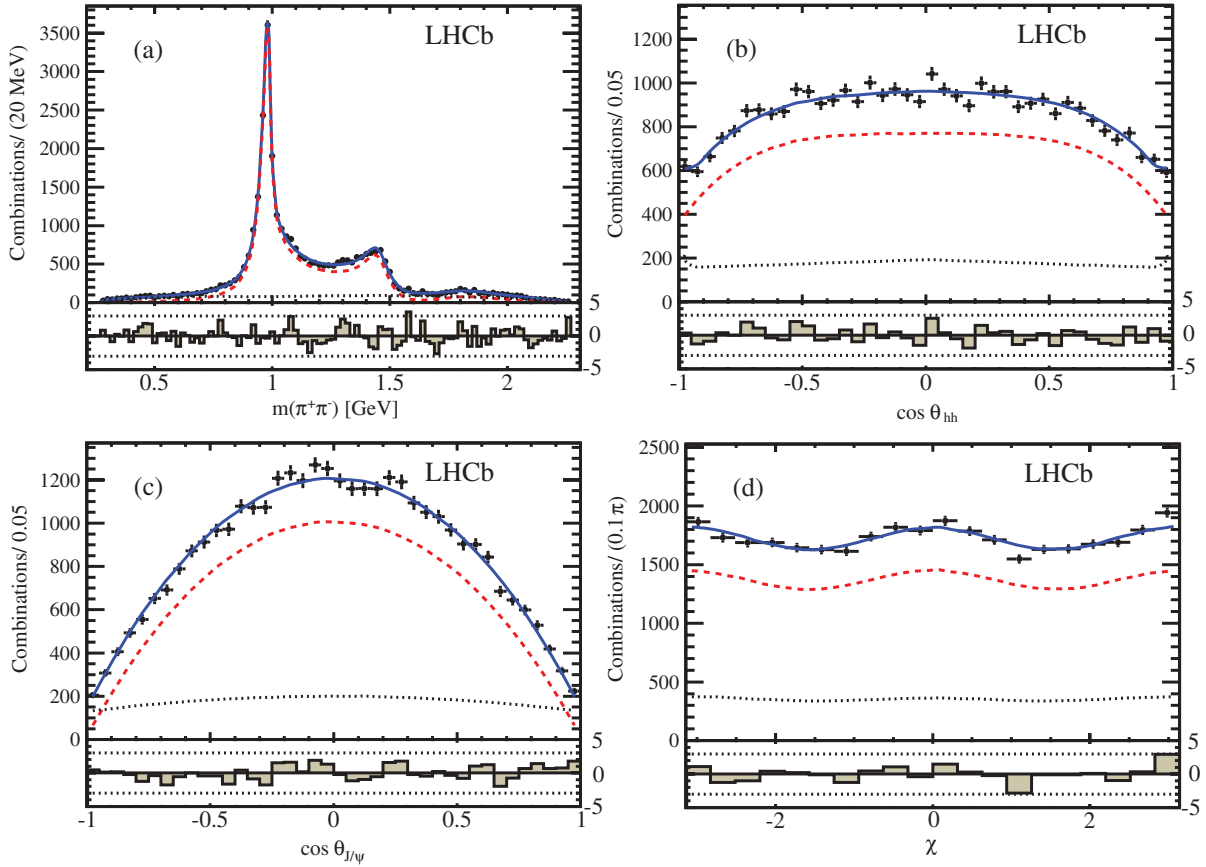


FIG. 14 (color online). Projections of (a) $m(\pi^+\pi^-)$, (b) $\cos \theta_{\pi\pi}$, (c) $\cos \theta_{J/\psi}$, and (d) χ for 5R Solution I. The points with error bars are data, the signal fit is shown with a (red) dashed line, the background is shown with a (black) dotted line, and the (blue) solid line represents the total.

and

$$\sum_{R,\tau} \mathcal{F}_\tau^R + \sum_{RR',\tau} \mathcal{F}_\tau^{RR'} = 1. \quad (24)$$

Interference between different spin- J states vanishes when integrated over angle, because the $d_{\lambda 0}^J$ angular functions are orthogonal.

C. Fit results

In order to compare the different models quantitatively, an estimate of the goodness of fit is calculated from four-dimensional (4D) partitions of the four variables, $m(\pi^+\pi^-)$, $\cos \theta_{hh}$, $\cos \theta_{J/\psi}$, and χ . We use the Poisson likelihood χ^2 [32], defined as

$$\chi^2 = 2 \sum_{i=1}^{N_{\text{bin}}} \left[x_i - n_i + n_i \ln \left(\frac{n_i}{x_i} \right) \right], \quad (25)$$

where n_i is the number of events in the four-dimensional bin i and x_i is the expected number of events in that bin according to the fitted likelihood function. A total of 1845 bins are used to calculate the χ^2 , where $41(m_{hh}) \times 5(\cos \theta_{hh}) \times 3(\cos \theta_{J/\psi}) \times 3(\chi)$ equal-size bins are used,

and m_{hh} is required to be between 0.25 and 2.30 GeV. The $\chi^2/\text{n.d.f.}$ and the negative of the logarithm of the likelihood, $-\ln \mathcal{L}$, of the fits are given in Table III, where n.d.f. is the number of degrees of freedom, given as 1845, subtracted by the number of fitting parameters and 1. The nomenclature describing the models gives the base model first and then “+” for any additions. The 5R model contains the resonances $f_0(980)$, $f_2(1270)$, $f_2'(1525)$, $f_0(1500)$, and $f_0(1790)$. In adding NR to the 5R model, two minima with similar likelihoods are found. One minimum is consistent with the 5R results and has a NR fit fraction of $(0.3 \pm 0.3)\%$; we group any fit models that are consistent with this 5R fit into the “Solution I” category. Another minimum has a significant NR fit fraction of $(5.9 \pm 1.4)\%$, this model and other consistent models are classified in the “Solution II” category.

Among these resonance models, we select the baseline model by requiring each resonance in the model to have more than 3 standard deviations (σ) of significance evaluated by the fit fraction divided by its uncertainty. The baseline fits are 5R in Solution I and 5R + NR in Solution II. No additional components are significant when added to these baseline fits. Unfortunately, we cannot distinguish between these two solutions and will

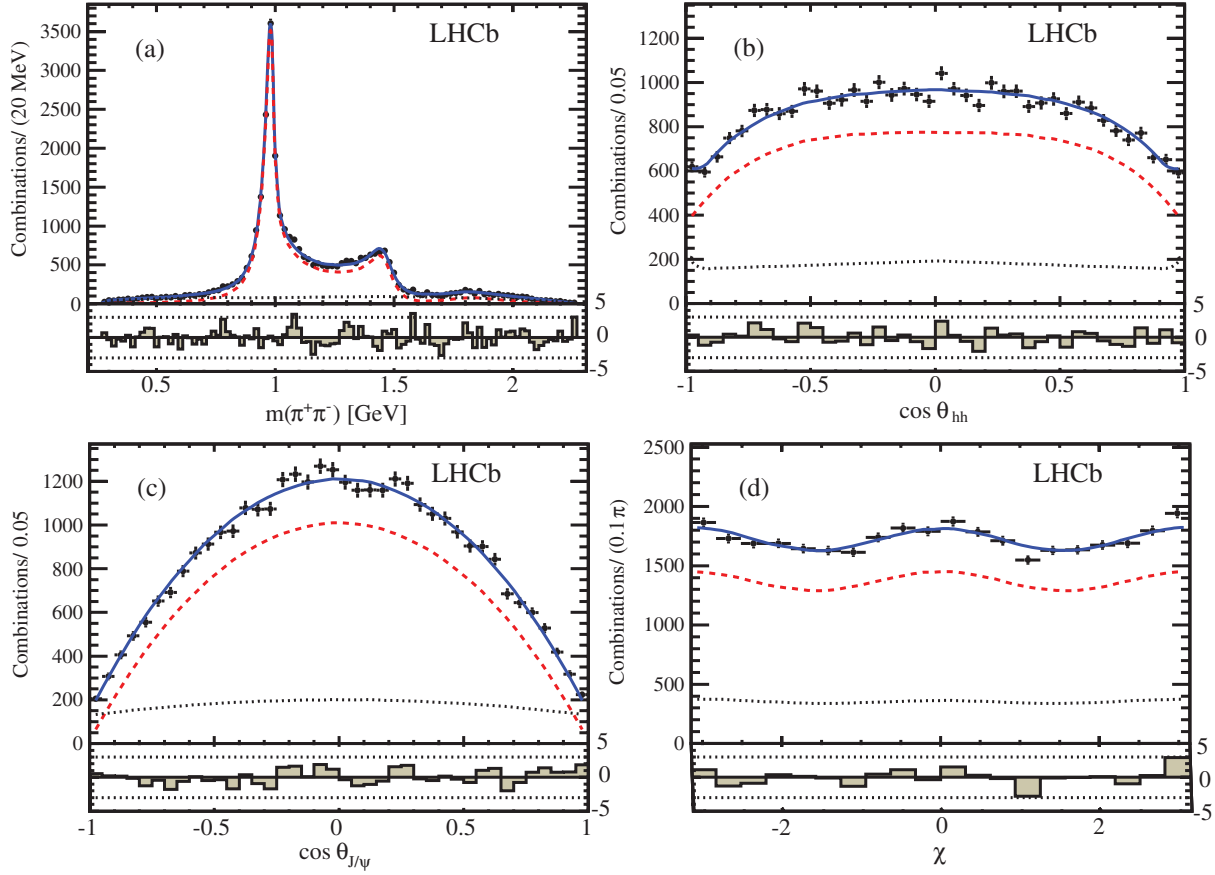


FIG. 15 (color online). Projections of (a) $m(\pi^+\pi^-)$, (b) $\cos \theta_{\pi\pi}$, (c) $\cos \theta_{J/\psi}$, and (d) χ for 5R + NR Solution II. The points with error bars are data, the signal fit is shown with a (red) dashed line, the background is shown with a (black) dotted line, and the (blue) solid line represents the total.

quote results for both of them. In both cases, the dominant contribution is S wave, including $f_0(980)$, $f_0(1500)$, and $f_0(1790)$. The D wave, $f_2(1270)$ and $f_2'(1525)$, is only 2.3% for both solutions.

Table IV shows the fit fractions from the baseline fits of two solutions, where systematic uncertainties are included; they will be discussed in Sec. VII. Figures 14 and 15 show the fit projections of $m(\pi^+\pi^-)$, $\cos \theta_{\pi\pi}$, $\cos \theta_{J/\psi}$ and χ from 5R Solution I and 5R + NR Solution II, respectively. Also shown in Figs. 16 and 17 are the contributions of each resonance as a function of $m(\pi^+\pi^-)$ from the baseline Solution I and II fits, respectively. Table V shows the fit fractions of the interference terms defined in Eq. (23). In addition, the phases are listed in Table VI. The other fit results are listed in Table VII, including the $f_0(980)$ mass, the Flatté function parameters $g_{\pi\pi}$, $g_{KK}/g_{\pi\pi}$, and masses and widths of $f_0(1500)$ and $f_0(1790)$ resonances.

In both solutions, the $f_0(500)$ state does not have a significant fit fraction. We set an upper limit for the fit fraction ratio between $f_0(500)$ and $f_0(980)$ of 0.3% from Solution I and 3.4% from Solution II, both at a 90% C.L. A similar situation is found for the $\rho(770)$ state. When including it in the fit, the fit fraction of $\rho(770)$ is measured

to be $(0.60 \pm 0.30^{+0.08}_{-0.14})\%$ in Solution I and $(1.02 \pm 0.36^{+0.09}_{-0.15})\%$ in Solution II. The largest upper limit is obtained by Solution II, where the $\rho(770)$ fit fraction is less than 1.7% at 90% C.L.

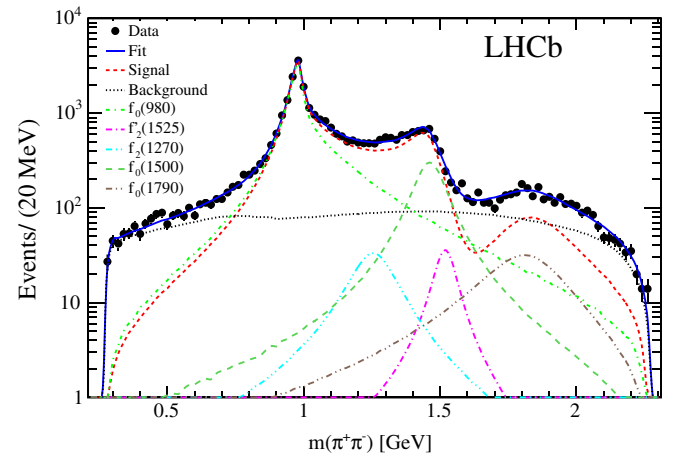


FIG. 16 (color online). Distribution of $m(\pi^+\pi^-)$ with contributing components labeled from 5R Solution I.

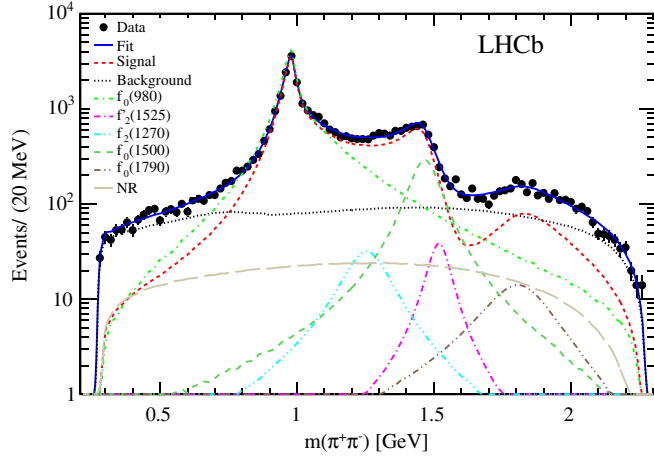


FIG. 17 (color online). Distribution of $m(\pi^+\pi^-)$ with contributing components labeled from 5R + NR Solution II.

Our previous study [3] did not consider the $f_0(1790)$ resonance; instead, the NR component filled in the higher-mass region near 1800 MeV. It is found that including $f_0(1790)$ improves the fit significantly in both solutions. Inclusion of this state reduces $-2 \ln \mathcal{L}$ by 276 (97) units and χ^2 by 213 (91) units with 4 additional n.d.f., corresponding to 14 (9) σ Gaussian significance, in Solution I (II), where the numbers are statistical only. When floating the parameters of $f_0(1790)$ resonance in the fits, we find its mass $m_{f_0(1790)} = 1815 \pm 23$ MeV and width $\Gamma_{f_0(1790)} = 353 \pm 48$ MeV in Solution I, and $m_{f_0(1790)} = 1793 \pm 26$ MeV and $\Gamma_{f_0(1790)} = 180 \pm 83$ MeV in Solution II, where the uncertainties are statistical only. The values in both solutions are consistent with the BES results $m_{f_0(1790)} = 1790^{+40}_{-30}$ MeV and $\Gamma_{f_0(1790)} = 270^{+60}_{-30}$ MeV [28] at the level of 1σ .

Figure 18 compares the total S-wave amplitude strength and phase as a function of $m(\pi^+\pi^-)$ between the two solutions, showing consistent amplitude strength but distinct phase. The total S-wave amplitude is calculated as Eq. (4) summing over all spin-0 component R with $\lambda = 0$, where the d function is equal to 1. The amplitude strength

TABLE V. Nonzero interference fraction (%) for both solutions.

Components	Solution I	Solution II
$f_0(980) + f_0(1500)$	9.50	-1.57
$f_0(980) + f_0(1790)$	7.93	5.30
$f_0(1500) + f_0(1790)$	-2.69	-2.26
$f_2(1270)_0 + f_2(1525)_0$	0.14	0.09
$f_2(1270)_\parallel + f_2'(1525)_\parallel$	-0.09	-0.16
$f_2(1270)_\perp + f_2'(1525)_\perp$	0.03	0.05
$f_0(980) + \text{NR}$...	-16.41
$f_0(1500) + \text{NR}$...	5.26
$f_0(1790) + \text{NR}$...	-0.95

TABLE VI. Fitted resonance phase differences ($^\circ$).

Resonance	Solution I	Solution II
$f_0(1500) - f_0(980)$	138 ± 4	177 ± 6
$f_0(1790) - f_0(980)$	78 ± 9	95 ± 16
$f_2(1270)_0 - f_0(980)$	96 ± 7	123 ± 8
$f_2(1270)_\parallel - f_0(980)$	-90 ± 11	-84 ± 13
$f_2'(1525)_0 - f_0(980)$	-132 ± 6	-97 ± 7
$f_2'(1525)_\parallel - f_0(980)$	103 ± 29	130 ± 20
NR $-f_0(980)$...	-104 ± 5
$f_2'(1525)_\perp - f_2(1270)_\perp$	149 ± 46	145 ± 51

TABLE VII. Other fit parameters. The uncertainties are only statistical.

Parameter	Solution I	Solution II
$m_{f_0(980)}$ (MeV)	945.4 ± 2.2	949.9 ± 2.1
$g_{\pi\pi}$ (MeV)	167 ± 7	167 ± 8
$g_{KK}/g_{\pi\pi}$	3.47 ± 0.12	3.05 ± 0.13
$m_{f_0(1500)}$ (MeV)	1460.9 ± 2.9	1465.9 ± 3.1
$\Gamma_{f_0(1500)}$ (MeV)	124 ± 7	115 ± 7
$m_{f_0(1790)}$ (MeV)	1814 ± 18	1809 ± 22
$\Gamma_{f_0(1790)}$ (MeV)	328 ± 34	263 ± 30

can be well measured from the $m(\pi^+\pi^-)$ distribution, but this is not the case for the phase, which is determined from the interference with the small fraction of higher spin resonances.

D. Angular moments

We define the moments of the cosine of the helicity angle $\theta_{\pi\pi}$, $\langle Y_l^0(\cos \theta_{\pi\pi}) \rangle$, as the efficiency-corrected and background-subtracted $\pi^+\pi^-$ invariant mass distributions, weighted by spherical harmonic functions. The moment distributions provide an additional way of visualizing the presence of different resonances and their interferences, similar to a partial wave analysis. Figures 19 and 20 show the distributions of the angular moments for 5R Solution I and 5R + NR Solution II, respectively. In general, the interpretation of these moments [3] is that $\langle Y_0^0 \rangle$ is the efficiency-corrected and background-subtracted event distribution, $\langle Y_1^0 \rangle$ is the interference of the sum of S-wave and P-wave and P-wave and D-wave amplitudes, $\langle Y_2^0 \rangle$ is the sum of the P-wave, D-wave and the interference of S-wave and D-wave amplitudes, $\langle Y_3^0 \rangle$ is the interference between the P-wave and D-wave amplitudes, $\langle Y_4^0 \rangle$ is D wave, and $\langle Y_5^0 \rangle$ is F wave. The values of $\langle Y_1^0 \rangle$ and $\langle Y_3^0 \rangle$ are almost zero, because the opposite contributions from B_s^0 and \bar{B}_s^0 decays are summed. Note that in this analysis, the P-wave contributions are zero, so the above description simplifies somewhat. The $f_2(1270)$ and $f_2'(1525)$ interference with S waves are clearly shown in the $\langle Y_2^0 \rangle$ plot [see Figs. 19(c) and 20(c)].

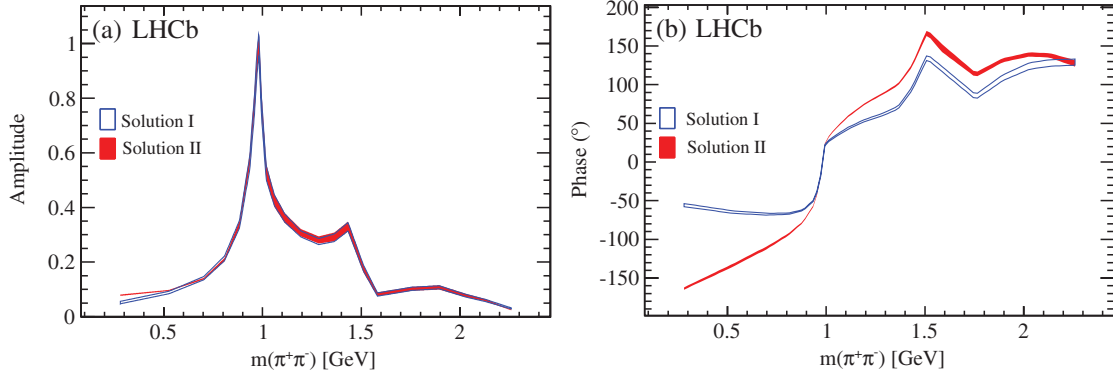


FIG. 18 (color online). S-wave (a) amplitude strength and (b) phase as a function of $m(\pi^+\pi^-)$ from the 5R Solution I (open) and 5R + NR Solution II (solid), where the widths of the curves reflect $\pm 1\sigma$ statistical uncertainties. The reference point is chosen at 980 MeV with amplitude strength equal to 1 and phase equal to 0.

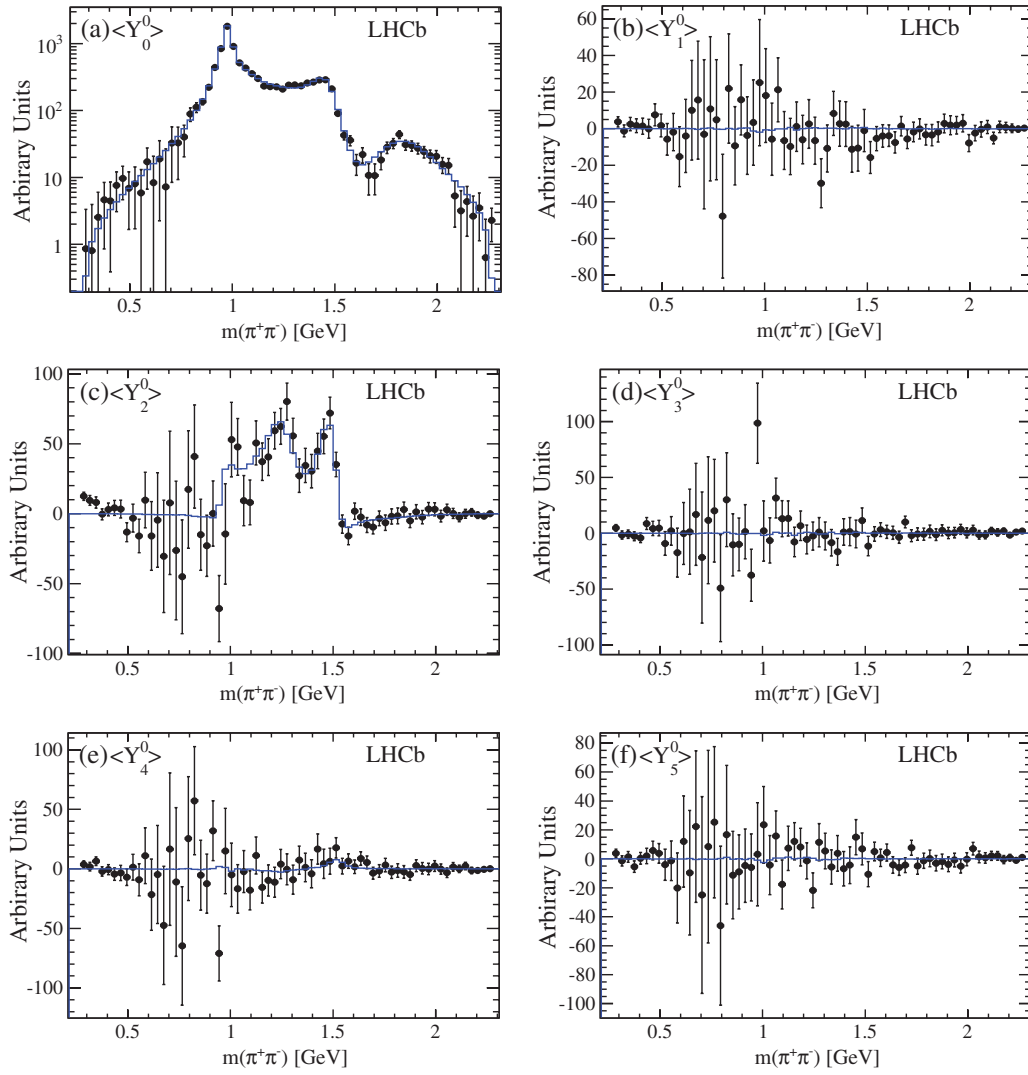


FIG. 19 (color online). The $\pi^+\pi^-$ mass dependence of the spherical harmonic moments of $\cos \theta_{\pi\pi}$ after efficiency corrections and background subtraction: (a) $\langle Y_0^0 \rangle$ ($\chi^2/\text{n.d.f.} = 78/70$), (b) $\langle Y_1^0 \rangle$ ($\chi^2/\text{n.d.f.} = 37/70$), (c) $\langle Y_2^0 \rangle$ ($\chi^2/\text{n.d.f.} = 79/70$), (d) $\langle Y_3^0 \rangle$ ($\chi^2/\text{n.d.f.} = 42/70$), (e) $\langle Y_4^0 \rangle$ ($\chi^2/\text{n.d.f.} = 43/70$), (f) $\langle Y_5^0 \rangle$ ($\chi^2/\text{n.d.f.} = 35/70$). The points with error bars are the data points, and the solid curves are derived from the model 5R Solution I.

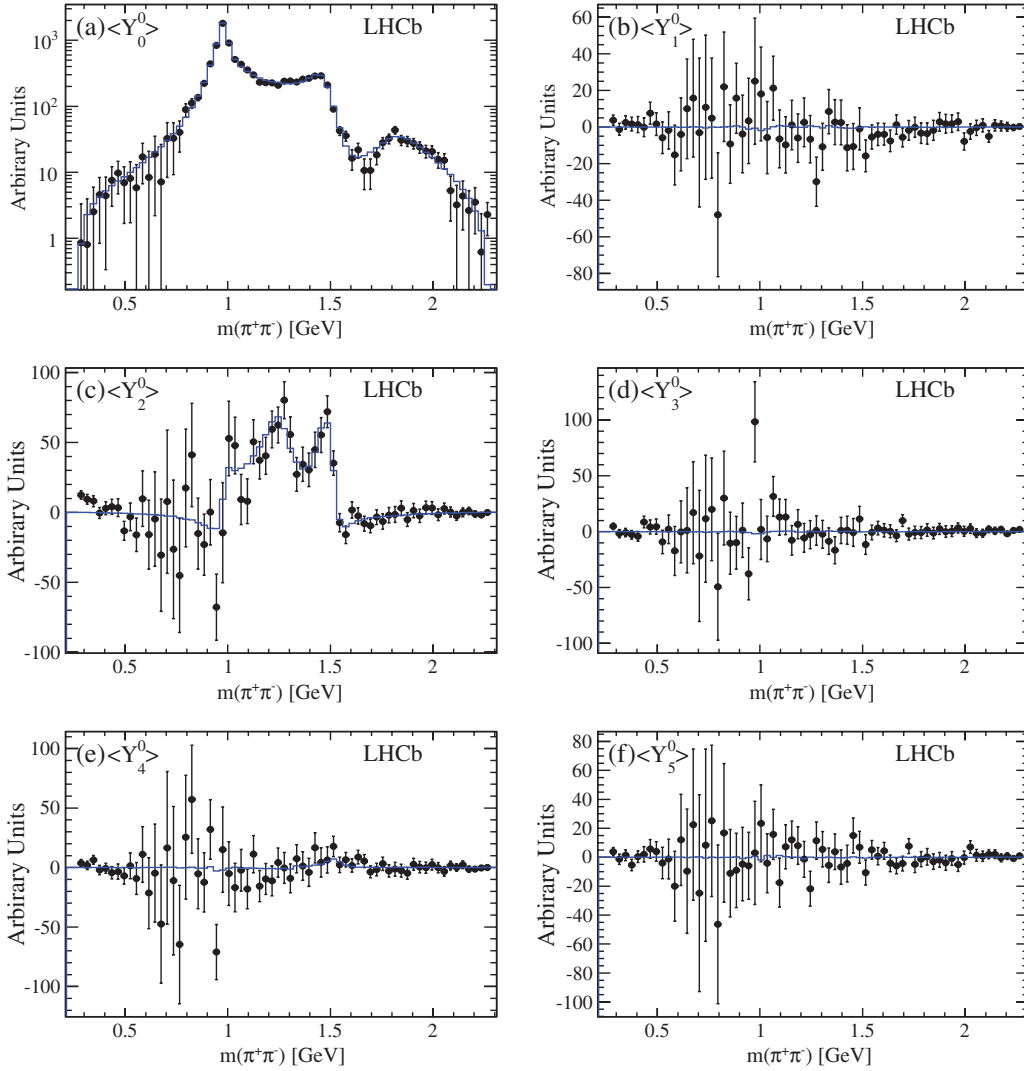


FIG. 20 (color online). The $\pi^+\pi^-$ mass dependence of the spherical harmonic moments of $\cos\theta_{\pi\pi}$ after efficiency corrections and background subtraction: (a) $\langle Y_0^0 \rangle$ ($\chi^2/\text{n.d.f.} = 73/70$), (b) $\langle Y_1^0 \rangle$ ($\chi^2/\text{n.d.f.} = 36/70$), (c) $\langle Y_2^0 \rangle$ ($\chi^2/\text{n.d.f.} = 72/70$), (d) $\langle Y_3^0 \rangle$ ($\chi^2/\text{n.d.f.} = 43/70$), (e) $\langle Y_4^0 \rangle$ ($\chi^2/\text{n.d.f.} = 41/70$), (f) $\langle Y_5^0 \rangle$ ($\chi^2/\text{n.d.f.} = 34/70$). The points with error bars are the data points, and the solid curves are derived from the model 5R + NR Solution II.

VII. SYSTEMATIC UNCERTAINTIES

The sources of the systematic uncertainties on the results of the amplitude analysis are summarized in Table VIII for Solution I and Table IX for Solution II. The contributions to the systematic error due to ϕ_s , the function $\varepsilon(t)$, Γ_s and $\Delta\Gamma_s$ [6] uncertainties, and L_B choices for transversity-0 and \parallel of spin ≥ 1 resonances are negligible. The systematic errors associated with the acceptance or background modeling are estimated by repeating the fit to the data 100 times. In each fit, the parameters in the acceptance or background function are randomly generated according to the corresponding error matrix. The uncertainties due to the fit model include possible contributions from each resonance listed in Table II but not used in the baseline fit models, varying the hadron scale r parameters in the Blatt-Weisskopf barrier

factors for both the B meson and R resonance from 5.0 GeV^{-1} and 1.5 GeV^{-1} , respectively, to 3.0 GeV^{-1} , and using $F_{KK} = 1$ in the Flatté function. Compared to the nominal Flatté function, the new one improves the likelihood fit $-2 \ln \mathcal{L}$ by 6.8 and 14.0 units for Solution I and Solution II, respectively. The largest variation among those changes is assigned as the systematic uncertainty for modeling.

We repeat the data fit by varying the mass and width of resonances within their errors one at a time and add the changes in quadrature. To assign a systematic uncertainty from the possible presence of the $f_0(500)$ or $\rho(770)$, we repeat the above procedures using the model that has the baseline resonances plus $f_0(500)$ or $\rho(770)$.

Finally, we have tested the entire procedure with simulated pseudoexperiments producing both the signal and

TABLE VIII. Absolute systematic uncertainties for Solution I.

Item	Acceptance	Background Fit fractions (%)	Fit model	Resonance parameters	Total
$f_0(980)$	± 0.17	± 0.36	$+0.00$ -5.04	± 0.03	$+0.4$ -5.1
$f_0(1500)$	± 0.06	± 0.14	$+1.11$ -0.29	± 0.02	$+1.1$ -0.3
$f_0(1790)$	± 0.02	± 0.11	$+4.98$ -0.11	± 0.01	$+5.0$ -0.2
$f_2(1270)_0$	± 0.03	± 0.01	± 0.01	± 0.01	± 0.03
$f_2(1270)_\parallel$	± 0.007	± 0.009	$+0.050$ -0.020	± 0.004	$+0.05$ -0.02
$f_2(1270)_\perp$	± 0.04	± 0.05	$+0.14$ -0.04	± 0.03	$+0.16$ -0.08
$f'_2(1525)_0$	± 0.007	± 0.012	$+0.030$ -0.000	± 0.03	$+0.05$ -0.04
$f'_2(1525)_\parallel$	± 0.003	± 0.004	$+0.000$ -0.020	± 0.004	$+0.05$ -0.02
$f'_2(1525)_\perp$	± 0.007	± 0.016	$+0.04$ -0.01	± 0.04	$+0.06$ -0.04
Other fraction (%)					
$f_0(500)/f_0(980)$	± 0.005	± 0.051	$+0.150$ -0.020	± 0.017	$+0.16$ -0.06
$\rho(770)$	± 0.013	± 0.065	$+0.040$ -0.120	± 0.013	$+0.08$ -0.14
CP -even	± 0.04	± 0.06	$+0.59$ -0.05	± 0.05	$+0.59$ -0.10

TABLE IX. Absolute systematic uncertainties for Solution II.

Item	Acceptance	Background Fit fractions (%)	Fit model	Resonance parameters	Total
$f_0(980)$	± 0.12	± 0.79	$+0.00$ -15.97	± 0.00	$+0.8$ -16.0
$f_0(1500)$	± 0.05	± 0.15	± 0.27	± 0.07	± 0.3
$f_0(1790)$	± 0.02	± 0.09	$+2.46$ -0.10	± 0.01	$+2.5$ -0.1
$f_2(1270)_0$	± 0.02	± 0.01	$+0.02$ -0.03	± 0.02	± 0.04
$f_2(1270)_\parallel$	± 0.005	± 0.009	$+0.110$ -0.010	± 0.020	$+0.11$ -0.02
$f_2(1270)_\perp$	± 0.04	± 0.05	$+0.10$ -0.05	± 0.03	$+0.12$ -0.09
$f'_2(1525)_0$	± 0.006	± 0.012	$+0.03$ -0.010	± 0.031	$+0.05$ -0.04
$f'_2(1525)_\parallel$	± 0.004	± 0.008	$+0.030$ -0.040	± 0.008	$+0.03$ -0.04
$f'_2(1525)_\perp$	± 0.01	± 0.02	$+0.03$ -0.00	± 0.05	$+0.06$ -0.05
NR	± 0.07	± 0.63	$+0.34$ -4.52	± 0.04	$+0.7$ -4.6
Other fraction (%)					
$f_0(500)/f_0(980)$	± 0.005	± 0.051	$+0.300$ -0.120	± 0.017	$+0.31$ -0.14
$\rho(770)$	± 0.015	± 0.080	$+0.040$ -0.120	± 0.016	$+0.09$ -0.15
CP -even	± 0.04	± 0.06	$+0.66$ -0.03	± 0.06	$+0.66$ -0.10

backgrounds and have verified that the fit finds the correct resonant substructure with the correct uncertainties.

VIII. FURTHER RESULTS

A. Fit fraction intervals

The fit fractions shown in Table IV differ considerably for some of the states between the two solutions. Table X lists the 1σ regions for the fit fractions, taking into account the differences between the solutions and including systematic uncertainties. The regions cover both 1σ intervals of the two solutions.

B. CP content

The only CP -even content arises from the \perp projections of the $f_2(1270)$ and $f'_2(1525)$ resonances, in addition to the 0 and \parallel of any possible $\rho(770)$ resonance. The CP -even measured values are $(0.89 \pm 0.38^{+0.59}_{-0.10})\%$ and $(0.86 \pm 0.42^{+0.66}_{-0.10})\%$ for Solutions I and II, respectively (see Table IV), where the systematic uncertainty is dominated by the forbidden $\rho(770)$ transversity-0 and \parallel components added in quadrature. To obtain the corresponding upper limit, the covariance matrix and parameter values from the fit are used to generate 2000 sample parameter sets. For each set, the CP -even fraction is calculated and is then

TABLE X. Fit fraction ranges, taking 1σ regions for both solutions, including systematic uncertainties.

Component	Fit fraction (%)
$f_0(980)$	65.0–94.5
$f_0(1500)$	8.2–11.5
$f_0(1790)$	0.6–7.4
$f_2(1270)_0$	0.28–0.50
$f_2(1270)_\parallel$	0.29–0.68
$f_2(1270)_\perp$	0.23–1.00
$f'_2(1525)_0$	0.41–0.62
$f'_2(1525)_\parallel$	0.02–0.27
$f'_2(1525)_\perp$	0.03–0.49
NR	0–7.5

smear by the systematic uncertainty. The integral of 95% of the area of the distribution yields an upper limit on the CP -even component of 2.3% at a 95% C.L., where the larger value given by Solution II is used. The upper limit is the same as our previous measurement [3], while the current measurement also adds in a possible $f'_2(1525)$ contribution.

C. Mixing angle and interpretation of light scalars

The $I = 0$ resonances, $f_0(500)$ and $f_0(980)$, are thought to be mixtures of underlying states whose mixing angle has been estimated previously (see references cited in Ref. [33]). The mixing is parametrized by a normal 2×2 rotation matrix characterized by the angle φ_m , giving in our case

$$\begin{aligned} |f_0(980)\rangle &= \cos \varphi_m |s\bar{s}\rangle + \sin \varphi_m |n\bar{n}\rangle, \\ |f_0(500)\rangle &= -\sin \varphi_m |s\bar{s}\rangle + \cos \varphi_m |n\bar{n}\rangle, \end{aligned}$$

where $|n\bar{n}\rangle \equiv \frac{1}{\sqrt{2}}(|u\bar{u}\rangle + |d\bar{d}\rangle)$. (26)

In this case, only the $|s\bar{s}\rangle$ wave function contributes. Thus, we have [2]

$$\tan^2 \varphi_m = \frac{\mathcal{B}(\bar{B}_s^0 \rightarrow J/\psi f_0(500)) \Phi(980)}{\mathcal{B}(\bar{B}_s^0 \rightarrow J/\psi f_0(980)) \Phi(500)}, \quad (27)$$

where the Φ 's are phase-space factors. The phase space in this pseudoscalar-to-vector-pseudoscalar decay is proportional to the cube of the f_0 momenta. Taking the average of the momentum-dependent phase space over the resonant line shapes results in the ratio of phase-space factors $\frac{\Phi(500)}{\Phi(980)} = 1.25$.

Our measured upper limit is

$$\frac{\mathcal{B}(\bar{B}_s^0 \rightarrow J/\psi f_0(500), f_0(500) \rightarrow \pi^+\pi^-)}{\mathcal{B}(\bar{B}_s^0 \rightarrow J/\psi f_0(980), f_0(980) \rightarrow \pi^+\pi^-)} < 3.4\% \quad (28)$$

at 90% C.L.,

where the larger value of the two solutions (II) is used. This value must be corrected for the individual branching

fractions of the f_0 resonances into $\pi^+\pi^-$. *BABAR* measures the relative branching ratios of $f_0(980) \rightarrow K^+K^-$ to $\pi^+\pi^-$ of 0.69 ± 0.32 using $B \rightarrow KKK$ and $B \rightarrow K\pi\pi$ decays [34]. BES has extracted relative branching ratios using $\psi(2S) \rightarrow \gamma\chi_{c0}$ decays where the $\chi_{c0} \rightarrow f_0(980)f_0(980)$, and either both $f_0(980)$'s decay into $\pi^+\pi^-$, or one decays into $\pi^+\pi^-$ and the other into K^+K^- [35]. Averaging the two measurements gives

$$\frac{\mathcal{B}(f_0(980) \rightarrow K^+K^-)}{\mathcal{B}(f_0(980) \rightarrow \pi^+\pi^-)} = 0.35^{+0.15}_{-0.14}. \quad (29)$$

Assuming that the $\pi\pi$ and KK decays are dominant, we can also extract

$$\mathcal{B}(f_0(980) \rightarrow \pi^+\pi^-) = (46 \pm 6)\%, \quad (30)$$

where we have assumed that the only other decays are to $\pi^0\pi^0$, $\frac{1}{2}$ of the $\pi^+\pi^-$ rate, and to neutral kaons, equal to charged kaons. We use $\mathcal{B}(f_0(500) \rightarrow \pi^+\pi^-) = \frac{2}{3}$, which results from isospin Clebsch-Gordon coefficients, assuming that the only decays are into two pions. Since we have only an upper limit on the $J/\psi f_0(500)$, we will only find an upper limit on the mixing angle, so if any other decay modes of the $f_0(500)$ exist, they would make the limit more stringent. Including the uncertainty of $\mathcal{B}(f_0(980) \rightarrow \pi^+\pi^-)$, our limit is

$$\tan^2 \varphi_m = \frac{\mathcal{B}(\bar{B}^0 \rightarrow J/\psi f_0(500)) \Phi(980)}{\mathcal{B}(\bar{B}^0 \rightarrow J/\psi f_0(980)) \Phi(500)} < 1.8\% \quad (31)$$

at 90% C.L.,

which translates into a limit

$$|\varphi_m| < 7.7^\circ \quad \text{at 90\% C.L.} \quad (32)$$

This limit is the most constraining ever placed on this mixing angle [19]. The value of $\tan^2 \varphi_m$ is consistent with the tetraquark model, which predicts zero within a few degrees [2,33].

IX. CONCLUSIONS

The $\bar{B}_s^0 \rightarrow J/\psi \pi^+\pi^-$ decay can be described by the interfering sum of five resonant components: $f_0(980)$, $f_0(1500)$, $f_0(1790)$, $f_2(1270)$, and $f'_2(1525)$. In addition, we find that a second model including these states plus nonresonant $J/\psi \pi^+\pi^-$ also provides a good description of the data. In both models, the largest component of the decay is the $f_0(980)$, with the $f_0(1500)$ being almost an order of magnitude smaller. We also find that including the $f_0(1790)$ resonance improves the data fit significantly. The $\pi^+\pi^-$ system is mostly S wave, with the D-wave components totaling only 2.3% in either model. No significant

$\bar{B}_s^0 \rightarrow J/\psi \rho(770)$ decay is observed; a 90% C.L. upper limit on the fit fraction is set to be 1.7%.

The most important result of this analysis is that the CP content is consistent with being purely odd, with the CP -even component limited to 2.3% at 95% C.L. Also of importance is the limit on the absolute value of the mixing angle between the $f_0(500)$ and $f_0(980)$ resonances of 7.7° at 90% C.L., the most stringent limit ever reported. This is also consistent with these states being tetraquarks.

ACKNOWLEDGMENTS

We express our gratitude to our colleagues in the CERN accelerator departments for the excellent performance of the LHC. We thank the technical and administrative staff at the LHCb institutes. We acknowledge support from CERN and from the national agencies: CAPES, CNPq, FAPERJ

and FINEP (Brazil); NSFC (China); CNRS/IN2P3 and Region Auvergne (France); BMBF, DFG, HGF and MPG (Germany); SFI (Ireland); INFN (Italy); FOM and NWO (Netherlands); SCSR (Poland); MEN/IFA (Romania); MinES, Rosatom, RFBR and NRC “Kurchatov Institute” (Russia); MinECo, XuntaGal and GENCAT (Spain); SNSF and SER (Switzerland); NAS Ukraine (Ukraine); STFC (United Kingdom); NSF (USA). We also acknowledge the support received from the ERC under FP7. The Tier1 computing centers are supported by IN2P3 (France), KIT and BMBF (Germany), INFN (Italy), NWO and SURF (Netherlands), PIC (Spain), GridPP (United Kingdom). We are indebted to the communities behind the multiple open-source software packages we depend on. We are also thankful for the computing resources and the access to software R&D tools provided by Yandex LLC (Russia).

-
- [1] R. Aaij *et al.* (LHCb Collaboration), *Phys. Rev. D* **87**, 112010 (2013).
 - [2] S. Stone and L. Zhang, *Phys. Rev. Lett.* **111**, 062001 (2013).
 - [3] R. Aaij *et al.* (LHCb Collaboration), *Phys. Rev. D* **86**, 052006 (2012).
 - [4] L. Zhang and S. Stone, *Phys. Lett. B* **719**, 383 (2013).
 - [5] I. I. Bigi and A. Sanda, *Cambridge Monogr. Part. Phys., Nucl. Phys., Cosmol.* **9**, 1 (2000).
 - [6] J. Beringer *et al.* (Particle Data Group), *Phys. Rev. D* **86**, 010001 (2012).
 - [7] R. Dalitz, *Philos. Mag.* **44**, 1068 (1953).
 - [8] A. A. Alves, Jr. *et al.* (LHCb Collaboration), *JINST* **3**, S08005 (2008).
 - [9] R. Arink *et al.*, *JINST* **9**, P01002 (2014).
 - [10] M. Adinolfi *et al.*, *Eur. Phys. J. C* **73**, 2431 (2013).
 - [11] A. A. Alves, Jr. *et al.*, *JINST* **8**, P02022 (2013).
 - [12] R. Aaij *et al.*, *JINST* **8**, P04022 (2013).
 - [13] T. Sjöstrand, S. Mrenna, and P. Skands, *J. High Energy Phys.* **05** (2006) 026 *Comput. Phys. Commun.* **178**, 852 (2008).
 - [14] I. Belyaev *et al.*, *Nuclear Science Symposium Conference Record (NSS/MIC)* (IEEE, New York, 2010), p. 1155.
 - [15] D. J. Lange, *Nucl. Instrum. Methods Phys. Res., Sect. A* **462**, 152 (2001).
 - [16] P. Golonka and Z. Was, *Eur. Phys. J. C* **45**, 97 (2006).
 - [17] J. Allison *et al.* (Geant4 Collaboration), *IEEE Trans. Nucl. Sci.* **53**, 270 (2006) S. Agostinelli *et al.* (Geant4 Collaboration), *Nucl. Instrum. Methods Phys. Res., Sect. A* **506**, 250 (2003).
 - [18] M. Clemencic, G. Corti, S. Easo, C. R. Jones, S. Miglioranzi, M. Pappagallo, and P. Robbe, *J. Phys. Conf. Ser.* **331**, 032023 (2011).
 - [19] R. Aaij *et al.* (LHCb Collaboration), *Phys. Rev. D* **87**, 052001 (2013).
 - [20] X. Cid Vidal, J. A. Hernando Morata, and B. Adeva Andany, Ph.D. thesis, Universidad de Santiago de Compostela, 2012.
 - [21] A. Hocker *et al.*, *Proc. Sci.*, ACAT (2007) 040.
 - [22] S. Stone and L. Zhang, [arXiv:0909.5442](https://arxiv.org/abs/0909.5442).
 - [23] R. Aaij *et al.* (LHCb Collaboration), *Phys. Lett. B* **713**, 378 (2012).
 - [24] J. Charles *et al.*, *Phys. Rev. D* **84**, 033005 (2011).
 - [25] R. Mizuk *et al.* (Belle Collaboration), *Phys. Rev. D* **80**, 031104 (2009).
 - [26] M. Ablikim *et al.* (BESIII Collaboration), *Phys. Rev. Lett.* **110**, 252001 (2013).
 - [27] R. Aaij *et al.* (LHCb Collaboration), *Phys. Rev. D* **87**, 072004 (2013).
 - [28] M. Ablikim *et al.* (BES Collaboration), *Phys. Lett. B* **607**, 243 (2005).
 - [29] W. Ochs, *J. Phys. G* **40**, 043001 (2013); *Acta Phys. Pol. B Proc. Suppl.* **6**, 839 (2013).
 - [30] D. V. Bugg, *Phys. Rev. D* **78**, 074023 (2008).
 - [31] S. M. Flatté, *Phys. Lett.* **63B**, 228 (1976).
 - [32] S. Baker and R. D. Cousins, *Nucl. Instrum. Methods Phys. Res.* **221**, 437 (1984).
 - [33] R. Fleischer, R. Knegjens, and G. Ricciardi, *Eur. Phys. J. C* **71**, 1832 (2011).
 - [34] B. Aubert *et al.* (BABAR Collaboration), *Phys. Rev. D* **74**, 032003 (2006).
 - [35] M. Ablikim *et al.* (BES Collaboration), *Phys. Rev. D* **70**, 092002 (2004) **72092002** (2005).
-

R. Aaij,⁴¹ B. Adeva,³⁷ M. Adinolfi,⁴⁶ A. Affolder,⁵² Z. Ajaltouni,⁵ J. Albrecht,⁹ F. Alessio,³⁸ M. Alexander,⁵¹ S. Ali,⁴¹ G. Alkhazov,³⁰ P. Alvarez Cartelle,³⁷ A. A. Alves Jr.,²⁵ S. Amato,² S. Amerio,²² Y. Amhis,⁷ L. Anderlini,^{17,a} J. Anderson,⁴⁰ R. Andreassen,⁵⁷ M. Andreotti,^{16,b} J. E. Andrews,⁵⁸ R. B. Appleby,⁵⁴ O. Aquines Gutierrez,¹⁰ F. Archilli,³⁸ A. Artamonov,³⁵ M. Artuso,⁵⁹ E. Aslanides,⁶ G. Auriemma,^{25,c} M. Baalouch,⁵ S. Bachmann,¹¹ J. J. Back,⁴⁸ A. Badalov,³⁶ V. Balagura,³¹ W. Baldini,¹⁶ R. J. Barlow,⁵⁴ C. Barschel,³⁹ S. Barsuk,⁷ W. Barter,⁴⁷ V. Batozskaya,²⁸ T. Bauer,⁴¹ A. Bay,³⁹ J. Beddow,⁵¹ F. Bedeschi,²³ I. Bediaga,¹ S. Belogurov,³¹ K. Belous,³⁵ I. Belyaev,³¹ E. Ben-Haim,⁸ G. Bencivenni,¹⁸ S. Benson,⁵⁰ J. Benton,⁴⁶ A. Berezhnuy,³² R. Bernet,⁴⁰ M.-O. Bettler,⁴⁷ M. van Beuzekom,⁴¹ A. Bien,¹¹ S. Bifani,⁴⁵ T. Bird,⁵⁴ A. Bizzeti,^{17,d} P. M. Bjørnstad,⁵⁴ T. Blake,⁴⁸ F. Blanc,³⁹ J. Blouw,¹⁰ S. Blusk,⁵⁹ V. Bocci,²⁵ A. Bondar,³⁴ N. Bondar,³⁰ W. Bonivento,^{15,38} S. Borghi,⁵⁴ A. Borgia,⁵⁹ M. Borsato,⁷ T. J. V. Bowcock,⁵² E. Bowen,⁴⁰ C. Bozzi,¹⁶ T. Brambach,⁹ J. van den Brand,⁴² J. Bressieux,³⁹ D. Brett,⁵⁴ M. Britsch,¹⁰ T. Britton,⁵⁹ N. H. Brook,⁴⁶ H. Brown,⁵² A. Bursche,⁴⁰ G. Busetto,^{22,e} J. Buytaert,³⁸ S. Cadetdu,¹⁵ R. Calabrese,^{16,b} O. Callot,⁷ M. Calvi,^{20,f} M. Calvo Gomez,^{36,g} A. Camboni,³⁶ P. Campana,^{18,38} D. Campora Perez,³⁸ A. Carbone,^{14,h} G. Carboni,^{24,i} R. Cardinale,^{19,j} A. Cardini,¹⁵ H. Carranza-Mejia,⁵⁰ L. Carson,⁵⁰ K. Carvalho Akiba,² G. Casse,⁵² L. Cassina,²⁰ L. Castillo Garcia,³⁸ M. Cattaneo,³⁸ C. Cauet,⁹ R. Cenci,⁵⁸ M. Charles,⁸ P. Charpentier,³⁸ S.-F. Cheung,⁵⁵ N. Chiapolini,⁴⁰ M. Chrzaszcz,^{40,26} K. Ciba,³⁸ X. Cid Vidal,³⁸ G. Ciezarek,⁵³ P. E. L. Clarke,⁵⁰ M. Clemencic,³⁸ H. V. Cliff,⁴⁷ J. Closier,³⁸ C. Coca,²⁹ V. Coco,³⁸ J. Cogan,⁶ E. Cogneras,⁵ P. Collins,³⁸ A. Comerma-Montells,³⁶ A. Contu,^{15,38} A. Cook,⁴⁶ M. Coombes,⁴⁶ S. Coquereau,⁸ G. Corti,³⁸ I. Counts,⁵⁶ B. Couturier,³⁸ G. A. Cowan,⁵⁰ D. C. Craik,⁴⁸ M. Cruz Torres,⁶⁰ S. Cunliffe,⁵³ R. Currie,⁵⁰ C. D'Ambrosio,³⁸ J. Dalseno,⁴⁶ P. David,⁸ P. N. Y. David,⁴¹ A. Davis,⁵⁷ I. De Bonis,⁴ K. De Bruyn,⁴¹ S. De Capua,⁵⁴ M. De Cian,¹¹ J. M. De Miranda,¹ L. De Paula,² W. De Silva,⁵⁷ P. De Simone,¹⁸ D. Decamp,⁴ M. Deckenhoff,⁹ L. Del Buono,⁸ N. Déléage,⁴ D. Derkach,⁵⁵ O. Deschamps,⁵ F. Dettori,⁴² A. Di Canto,¹¹ H. Dijkstra,³⁸ S. Donleavy,⁵² F. Dordei,¹¹ M. Dorigo,³⁹ P. Dorosz,^{26,k} A. Dosil Suárez,³⁷ D. Dossett,⁴⁸ A. Dovbnya,⁴³ F. Dupertuis,³⁹ P. Durante,³⁸ R. Dzhelyadin,³⁵ A. Dziurda,²⁶ A. Dzyuba,³⁰ S. Easo,⁴⁹ U. Egede,⁵³ V. Egorychev,³¹ S. Eidelman,³⁴ S. Eisenhardt,⁵⁰ U. Eitschberger,⁹ R. Ekelhof,⁹ L. Eklund,^{51,38} I. El Rifai,⁵ C. Elsasser,⁴⁰ S. Esen,¹¹ A. Falabella,^{16,b} C. Färber,¹¹ C. Farinelli,⁴¹ S. Farry,⁵² D. Ferguson,⁵⁰ V. Fernandez Albor,³⁷ F. Ferreira Rodrigues,¹ M. Ferro-Luzzi,³⁸ S. Filippov,³³ M. Fiore,^{16,b} M. Fiorini,^{16,b} C. Fitzpatrick,³⁸ M. Fontana,¹⁰ F. Fontanelli,^{19,j} R. Forty,³⁸ O. Francisco,² M. Frank,³⁸ C. Frei,³⁸ M. Frosini,^{17,38,a} J. Fu,²¹ E. Furfaro,^{24,i} A. Gallas Torreira,³⁷ D. Galli,^{14,h} M. Gandelman,² P. Gandini,⁵⁹ Y. Gao,³ J. Garofoli,⁵⁹ J. Garra Tico,⁴⁷ L. Garrido,³⁶ C. Gaspar,³⁸ R. Gauld,⁵⁵ L. Gavardi,⁹ E. Gersabeck,¹¹ M. Gersabeck,⁵⁴ T. Gershon,⁴⁸ P. Ghez,⁴ A. Gianelle,²² S. Giani,³⁹ V. Gibson,⁴⁷ L. Giubega,²⁹ V. V. Gligorov,³⁸ C. Göbel,⁶⁰ D. Golubkov,³¹ A. Golutvin,^{53,31,38} A. Gomes,^{1,l} H. Gordon,³⁸ M. Grabalosa Gándara,⁵ R. Graciani Diaz,³⁶ L. A. Granado Cardoso,³⁸ E. Graugés,³⁶ G. Graziani,¹⁷ A. Grecu,²⁹ E. Greening,⁵⁵ S. Gregson,⁴⁷ P. Griffith,⁴⁵ L. Grillo,¹¹ O. Grünberg,⁶¹ B. Gui,⁵⁹ E. Gushchin,³³ Y. Guz,^{35,38} T. Gys,³⁸ C. Hadjivasiliou,⁵⁹ G. Haefeli,³⁹ C. Haen,³⁸ T. W. Hafkenscheid,⁶⁴ S. C. Haines,⁴⁷ S. Hall,⁵³ B. Hamilton,⁵⁸ T. Hampson,⁴⁶ S. Hansmann-Menzemer,¹¹ N. Harnew,⁵⁵ S. T. Harnew,⁴⁶ J. Harrison,⁵⁴ T. Hartmann,⁶¹ J. He,³⁸ T. Head,³⁸ V. Heijne,⁴¹ K. Hennessy,⁵² P. Henrard,⁵ L. Henry,⁸ J. A. Hernando Morata,³⁷ E. van Herwijnen,³⁸ M. Heß,⁶¹ A. Hicheur,¹ D. Hill,⁵⁵ M. Hoballah,⁵ C. Hombach,⁵⁴ W. Hulsbergen,⁴¹ P. Hunt,⁵⁵ N. Hussain,⁵⁵ D. Hutchcroft,⁵² D. Hynds,⁵¹ V. Iakovenko,⁴⁴ M. Idzik,²⁷ P. Ilten,⁵⁶ R. Jacobsson,³⁸ A. Jaeger,¹¹ E. Jans,⁴¹ P. Jaton,³⁹ A. Jawahery,⁵⁸ F. Jing,³ M. John,⁵⁵ D. Johnson,⁵⁵ C. R. Jones,⁴⁷ C. Joram,³⁸ B. Jost,³⁸ N. Jurik,⁵⁹ M. Kaballo,⁹ S. Kandybei,⁴³ W. Kanso,⁶ M. Karacson,³⁸ T. M. Karbach,³⁸ M. Kelsey,⁵⁹ I. R. Kenyon,⁴⁵ T. Ketel,⁴² B. Khanji,²⁰ C. Khurewathanakul,³⁹ S. Klaver,⁵⁴ O. Kochebina,⁷ I. Komarov,³⁹ R. F. Koopman,⁴² P. Koppenburg,⁴¹ M. Korolev,³² A. Kozlinskiy,⁴¹ L. Kravchuk,³³ K. Kreplin,¹¹ M. Kreps,⁴⁸ G. Krocker,¹¹ P. Krokovny,³⁴ F. Kruse,⁹ M. Kucharczyk,^{20,26,38,f} V. Kudryavtsev,³⁴ K. Kurek,²⁸ T. Kvaratskheliya,^{31,38} V. N. La Thi,³⁹ D. Lacarrere,³⁸ G. Lafferty,⁵⁴ A. Lai,¹⁵ D. Lambert,⁵⁰ R. W. Lambert,⁴² E. Lanciotti,³⁸ G. Lanfranchi,¹⁸ C. Langenbruch,³⁸ T. Latham,⁴⁸ C. Lazzeroni,⁴⁵ R. Le Gac,⁶ J. van Leerdam,⁴¹ J.-P. Lees,⁴ R. Lefèvre,⁵ A. Leflat,³² J. Lefrançois,⁷ S. Leo,²³ O. Leroy,⁶ T. Lesiak,²⁶ B. Leverington,¹¹ Y. Li,³ M. Liles,⁵² R. Lindner,³⁸ C. Linn,³⁸ F. Lionetto,⁴⁰ B. Liu,¹⁵ G. Liu,³⁸ S. Lohn,³⁸ I. Longstaff,⁵¹ J. H. Lopes,² N. Lopez-March,³⁹ P. Lowdon,⁴⁰ H. Lu,³ D. Lucchesi,^{22,e} J. Luisier,³⁹ H. Luo,⁵⁰ E. Luppi,^{16,b} O. Lupton,⁵⁵ F. Machefert,⁷ I. V. Machikhiliyan,³¹ F. Maciuc,²⁹ O. Maev,^{30,38} S. Malde,⁵⁵ G. Manca,^{15,m} G. Mancinelli,⁶ M. Manzali,^{16,b} J. Maratas,⁵ U. Marconi,¹⁴ P. Marino,^{23,n} R. Märki,³⁹ J. Marks,¹¹ G. Martellotti,²⁵ A. Martens,⁸ A. Martín Sánchez,⁷ M. Martinelli,⁴¹ D. Martinez Santos,⁴² F. Martinez Vidal,⁶³ D. Martins Tostes,² A. Massafferri,¹ R. Matev,³⁸ Z. Mathe,³⁸ C. Matteuzzi,²⁰ A. Mazurov,^{16,38,b} M. McCann,⁵³ J. McCarthy,⁴⁵ A. McNab,⁵⁴ R. McNulty,¹² B. McKelley,⁵² B. Meadows,^{57,55} F. Meier,⁹ M. Meissner,¹¹ M. Merk,⁴¹ D. A. Milanese,⁸ M.-N. Minard,⁴ J. Molina Rodriguez,⁶⁰ S. Monteil,⁵ D. Moran,⁵⁴ M. Morandin,²² P. Morawski,²⁶ A. Mordà,⁶ M. J. Morello,^{23,n} R. Mountain,⁵⁹ F. Muheim,⁵⁰ K. Müller,⁴⁰

R. Muresan,²⁹ B. Muryn,²⁷ B. Muster,³⁹ P. Naik,⁴⁶ T. Nakada,³⁹ R. Nandakumar,⁴⁹ I. Nasteva,¹ M. Needham,⁵⁰ N. Neri,²¹ S. Neubert,³⁸ N. Neufeld,³⁸ A. D. Nguyen,³⁹ T. D. Nguyen,³⁹ C. Nguyen-Mau,^{39,o} M. Nicol,⁷ V. Niess,⁵ R. Niet,⁹ N. Nikitin,³² T. Nikodem,¹¹ A. Novoselov,³⁵ A. Oblakowska-Mucha,²⁷ V. Obraztsov,³⁵ S. Oggero,⁴¹ S. Ogilvy,⁵¹ O. Okhrimenko,⁴⁴ R. Oldeman,^{15,m} G. Onderwater,⁶⁴ M. Orlandea,²⁹ J. M. Otalora Goicochea,² P. Owen,⁵³ A. Oyanguren,³⁶ B. K. Pal,⁵⁹ A. Palano,^{13,p} F. Palombo,^{21,q} M. Palutan,¹⁸ J. Panman,³⁸ A. Papanestis,^{49,38} M. Pappagallo,⁵¹ L. Pappalardo,¹⁶ C. Parkes,⁵⁴ C. J. Parkinson,⁹ G. Passaleva,¹⁷ G. D. Patel,⁵² M. Patel,⁵³ C. Patrignani,^{19,j} C. Pavel-Nicorescu,²⁹ A. Pazos Alvarez,³⁷ A. Pearce,⁵⁴ A. Pellegrino,⁴¹ G. Penso,^{25,r} M. Pepe Altarelli,³⁸ S. Perazzini,^{14,h} E. Perez Trigo,³⁷ P. Perret,⁵ M. Perrin-Terrin,⁶ L. Pescatore,⁴⁵ E. Pesen,⁶⁵ G. Pessina,²⁰ K. Petridis,⁵³ A. Petrolini,^{19,j} E. Picatoste Olloqui,³⁶ B. Pietrzyk,⁴ T. Pilař,⁴⁸ D. Pinci,²⁵ A. Pistone,¹⁹ S. Playfer,⁵⁰ M. Plo Casasus,³⁷ F. Polci,⁸ G. Polok,²⁶ A. Poluektov,^{48,34} E. Polcarpo,² A. Popov,³⁵ D. Popov,¹⁰ B. Popovici,²⁹ C. Potterat,³⁶ A. Powell,⁵⁵ J. Prisciandaro,³⁹ A. Pritchard,⁵² C. Prouve,⁴⁶ V. Pugatch,⁴⁴ A. Puig Navarro,³⁹ G. Punzi,^{23,s} W. Qian,⁴ B. Rachwal,²⁶ J. H. Rademacker,⁴⁶ B. Rakotomiamanana,³⁹ M. Rama,¹⁸ M. S. Rangel,² I. Raniuk,⁴³ N. Rauschmayr,³⁸ G. Raven,⁴² S. Redford,⁵⁵ S. Reichert,⁵⁴ M. M. Reid,⁴⁸ A. C. dos Reis,¹ S. Ricciardi,⁴⁹ A. Richards,⁵³ K. Rinnert,⁵² V. Rives Molina,³⁶ D. A. Roa Romero,⁵ P. Robbe,⁷ D. A. Roberts,⁵⁸ A. B. Rodrigues,¹ E. Rodrigues,⁵⁴ P. Rodriguez Perez,³⁷ S. Roiser,³⁸ V. Romanovsky,³⁵ A. Romero Vidal,³⁷ M. Rotondo,²² J. Rouvinet,³⁹ T. Ruf,³⁸ F. Ruffini,²³ H. Ruiz,³⁶ P. Ruiz Valls,³⁶ G. Sabatino,^{25,i} J. J. Saborido Silva,³⁷ N. Sagidova,³⁰ P. Sail,⁵¹ B. Saitta,^{15,m} V. Salustino Guimaraes,² B. Sanmartin Sedes,³⁷ R. Santacesaria,²⁵ C. Santamarina Rios,³⁷ E. Santovetti,^{24,i} M. Sapunov,⁶ A. Sarti,¹⁸ C. Satriano,^{25,c} A. Satta,²⁴ M. Savrie,^{16,b} D. Savrina,^{31,32} M. Schiller,⁴² H. Schindler,³⁸ M. Schlupp,⁹ M. Schmelling,¹⁰ B. Schmidt,³⁸ O. Schneider,³⁹ A. Schopper,³⁸ M.-H. Schune,⁷ R. Schwemmer,³⁸ B. Sciascia,¹⁸ A. Sciubba,²⁵ M. Seco,³⁷ A. Semennikov,³¹ K. Senderowska,²⁷ I. Sepp,⁵³ N. Serra,⁴⁰ J. Serrano,⁶ P. Seyfert,¹¹ M. Shapkin,³⁵ I. Shapoval,^{16,43,b} Y. Shcheglov,³⁰ T. Shears,⁵² L. Shekhtman,³⁴ O. Shevchenko,⁴³ V. Shevchenko,⁶² A. Shires,⁹ R. Silva Coutinho,⁴⁸ G. Simi,²² M. Sirendi,⁴⁷ N. Skidmore,⁴⁶ T. Skwarnicki,⁵⁹ N. A. Smith,⁵² E. Smith,^{55,49} E. Smith,⁵³ J. Smith,⁴⁷ M. Smith,⁵⁴ H. Snoek,⁴¹ M. D. Sokoloff,⁵⁷ F. J. P. Soler,⁵¹ F. Soomro,³⁹ D. Souza,⁴⁶ B. Souza De Paula,² B. Spaan,⁹ A. Sparkes,⁵⁰ F. Spinella,²³ P. Spradlin,⁵¹ F. Stagni,³⁸ S. Stahl,¹¹ O. Steinkamp,⁴⁰ S. Stevenson,⁵⁵ S. Stoica,²⁹ S. Stone,⁵⁹ B. Storaci,⁴⁰ S. Stracka,^{23,38} M. Straticiuc,²⁹ U. Straumann,⁴⁰ R. Stroili,²² V. K. Subbiah,³⁸ L. Sun,⁵⁷ W. Sutcliffe,⁵³ S. Swientek,⁹ V. Syropoulos,⁴² M. Szczekowski,²⁸ P. Szczypka,^{39,38} D. Szilard,² T. Szumlak,²⁷ S. T'Jampens,⁴ M. Teklishyn,⁷ G. Tellarini,^{16,b} E. Teodorescu,²⁹ F. Teubert,³⁸ C. Thomas,⁵⁵ E. Thomas,³⁸ J. van Tilburg,¹¹ V. Tisserand,⁴ M. Tobin,³⁹ S. Tolk,⁴² L. Tomassetti,^{16,b} D. Tonelli,³⁸ S. Topp-Joergensen,⁵⁵ N. Torr,⁵⁵ E. Tournefier,^{4,53} S. Tourneur,³⁹ M. T. Tran,³⁹ M. Tresch,⁴⁰ A. Tsaregorodtsev,⁶ P. Tsopelas,⁴¹ N. Tuning,⁴¹ M. Ubeda Garcia,³⁸ A. Ukleja,²⁸ A. Ustyuzhanin,⁶² U. Uwer,¹¹ V. Vagnoni,¹⁴ G. Valenti,¹⁴ A. Vallier,⁷ R. Vazquez Gomez,¹⁸ P. Vazquez Regueiro,³⁷ C. Vázquez Sierra,³⁷ S. Vecchi,¹⁶ J. J. Velthuis,⁴⁶ M. Veltri,^{17,t} G. Veneziano,³⁹ M. Vesterinen,¹¹ B. Viaud,⁷ D. Vieira,² X. Vilasis-Cardona,^{36,g} A. Vollhardt,⁴⁰ D. Volyanskyy,¹⁰ D. Voong,⁴⁶ A. Vorobyev,³⁰ V. Vorobyev,³⁴ C. Voß,⁶¹ H. Voss,¹⁰ J. A. de Vries,⁴¹ R. Waldi,⁶¹ C. Wallace,⁴⁸ R. Wallace,¹² S. Wandernoth,¹¹ J. Wang,⁵⁹ D. R. Ward,⁴⁷ N. K. Watson,⁴⁵ A. D. Webber,⁵⁴ D. Websdale,⁵³ M. Whitehead,⁴⁸ J. Wicht,³⁸ J. Wiechczynski,²⁶ D. Wiedner,¹¹ L. Wiggers,⁴¹ G. Wilkinson,⁵⁵ M. P. Williams,^{48,49} M. Williams,⁵⁶ F. F. Wilson,⁴⁹ J. Wimberley,⁵⁸ J. Wishahi,⁹ W. Wislicki,²⁸ M. Witek,²⁶ G. Wormser,⁷ S. A. Wotton,⁴⁷ S. Wright,⁴⁷ S. Wu,³ K. Wyllie,³⁸ Y. Xie,^{50,38} Z. Xing,⁵⁹ Z. Yang,³ X. Yuan,³ O. Yushchenko,³⁵ M. Zangoli,¹⁴ M. Zavertyaev,^{10,u} F. Zhang,³ L. Zhang,⁵⁹ W. C. Zhang,¹² Y. Zhang,³ A. Zhelezov,¹¹ A. Zhokhov,³¹ L. Zhong³ and A. Zvyagin³⁸

(LHCb Collaboration)

¹Centro Brasileiro de Pesquisas Físicas (CBPF), Rio de Janeiro, Brazil²Universidade Federal do Rio de Janeiro (UFRJ), Rio de Janeiro, Brazil³Center for High Energy Physics, Tsinghua University, Beijing, China⁴LAPP, Université de Savoie, CNRS/IN2P3, Annecy-Le-Vieux, France⁵Clermont Université, Université Blaise Pascal, CNRS/IN2P3, LPC, Clermont-Ferrand, France⁶CPM, Aix-Marseille Université, CNRS/IN2P3, Marseille, France⁷LAL, Université Paris-Sud, CNRS/IN2P3, Orsay, France⁸LPNHE, Université Pierre et Marie Curie, Université Paris Diderot, CNRS/IN2P3, Paris, France⁹Fakultät Physik, Technische Universität Dortmund, Dortmund, Germany¹⁰Max-Planck-Institut für Kernphysik (MPIK), Heidelberg, Germany¹¹Physikalisches Institut, Ruprecht-Karls-Universität Heidelberg, Heidelberg, Germany

- ¹²*School of Physics, University College Dublin, Dublin, Ireland*
- ¹³*Sezione INFN di Bari, Bari, Italy*
- ¹⁴*Sezione INFN di Bologna, Bologna, Italy*
- ¹⁵*Sezione INFN di Cagliari, Cagliari, Italy*
- ¹⁶*Sezione INFN di Ferrara, Ferrara, Italy*
- ¹⁷*Sezione INFN di Firenze, Firenze, Italy*
- ¹⁸*Laboratori Nazionali dell'INFN di Frascati, Frascati, Italy*
- ¹⁹*Sezione INFN di Genova, Genova, Italy*
- ²⁰*Sezione INFN di Milano Bicocca, Milano, Italy*
- ²¹*Sezione INFN di Milano, Milano, Italy*
- ²²*Sezione INFN di Padova, Padova, Italy*
- ²³*Sezione INFN di Pisa, Pisa, Italy*
- ²⁴*Sezione INFN di Roma Tor Vergata, Roma, Italy*
- ²⁵*Sezione INFN di Roma La Sapienza, Roma, Italy*
- ²⁶*Henryk Niewodniczanski Institute of Nuclear Physics Polish Academy of Sciences, Kraków, Poland*
- ²⁷*AGH - University of Science and Technology, Faculty of Physics and Applied Computer Science, Kraków, Poland*
- ²⁸*National Center for Nuclear Research (NCBJ), Warsaw, Poland*
- ²⁹*Horia Hulubei National Institute of Physics and Nuclear Engineering, Bucharest-Magurele, Romania*
- ³⁰*Petersburg Nuclear Physics Institute (PNPI), Gatchina, Russia*
- ³¹*Institute of Theoretical and Experimental Physics (ITEP), Moscow, Russia*
- ³²*Institute of Nuclear Physics, Moscow State University (SINP MSU), Moscow, Russia*
- ³³*Institute for Nuclear Research of the Russian Academy of Sciences (INR RAN), Moscow, Russia*
- ³⁴*Budker Institute of Nuclear Physics (SB RAS) and Novosibirsk State University, Novosibirsk, Russia*
- ³⁵*Institute for High Energy Physics (IHEP), Protvino, Russia*
- ³⁶*Universitat de Barcelona, Barcelona, Spain*
- ³⁷*Universidad de Santiago de Compostela, Santiago de Compostela, Spain*
- ³⁸*European Organization for Nuclear Research (CERN), Geneva, Switzerland*
- ³⁹*Ecole Polytechnique Fédérale de Lausanne (EPFL), Lausanne, Switzerland*
- ⁴⁰*Physik-Institut, Universität Zürich, Zürich, Switzerland*
- ⁴¹*Nikhef National Institute for Subatomic Physics, Amsterdam, The Netherlands*
- ⁴²*Nikhef National Institute for Subatomic Physics and VU University Amsterdam, Amsterdam, The Netherlands*
- ⁴³*NSC Kharkiv Institute of Physics and Technology (NSC KIPT), Kharkiv, Ukraine*
- ⁴⁴*Institute for Nuclear Research of the National Academy of Sciences (KINR), Kyiv, Ukraine*
- ⁴⁵*University of Birmingham, Birmingham, United Kingdom*
- ⁴⁶*H.H. Wills Physics Laboratory, University of Bristol, Bristol, United Kingdom*
- ⁴⁷*Cavendish Laboratory, University of Cambridge, Cambridge, United Kingdom*
- ⁴⁸*Department of Physics, University of Warwick, Coventry, United Kingdom*
- ⁴⁹*STFC Rutherford Appleton Laboratory, Didcot, United Kingdom*
- ⁵⁰*School of Physics and Astronomy, University of Edinburgh, Edinburgh, United Kingdom*
- ⁵¹*School of Physics and Astronomy, University of Glasgow, Glasgow, United Kingdom*
- ⁵²*Oliver Lodge Laboratory, University of Liverpool, Liverpool, United Kingdom*
- ⁵³*Imperial College London, London, United Kingdom*
- ⁵⁴*School of Physics and Astronomy, University of Manchester, Manchester, United Kingdom*
- ⁵⁵*Department of Physics, University of Oxford, Oxford, United Kingdom*
- ⁵⁶*Massachusetts Institute of Technology, Cambridge, Massachusetts, USA*
- ⁵⁷*University of Cincinnati, Cincinnati, Ohio, USA*
- ⁵⁸*University of Maryland, College Park, Maryland, USA*
- ⁵⁹*Syracuse University, Syracuse, New York, USA*
- ⁶⁰*Pontificia Universidade Católica do Rio de Janeiro (PUC-Rio), Rio de Janeiro, Brazil
(associated with Universidade Federal do Rio de Janeiro (UFRJ),
Rio de Janeiro, Brazil)*
- ⁶¹*Institut für Physik, Universität Rostock, Rostock, Germany
(associated with Physikalisches Institut, Ruprecht-Karls-Universität Heidelberg, Heidelberg, Germany)*
- ⁶²*National Research Centre Kurchatov Institute, Moscow, Russia (associated with Institute of Theoretical
and Experimental Physics (ITEP), Moscow, Russia)*
- ⁶³*Instituto de Física Corpuscular (IFIC), Universitat de Valencia-CSIC, Valencia, Spain (associated with
Universitat de Barcelona, Barcelona, Spain)*

⁶⁴*KVI - University of Groningen, Groningen, The Netherlands (associated with Nikhef National Institute for Subatomic Physics, Amsterdam, The Netherlands)*

⁶⁵*Celal Bayar University, Manisa, Turkey (associated with European Organization for Nuclear Research (CERN), Geneva, Switzerland)*

^aAlso at Università di Firenze, Firenze, Italy.

^bAlso at Università di Ferrara, Ferrara, Italy.

^cAlso at Università della Basilicata, Potenza, Italy.

^dAlso at Università di Modena e Reggio Emilia, Modena, Italy.

^eAlso at Università di Padova, Padova, Italy.

^fAlso at Università di Milano Bicocca, Milano, Italy.

^gAlso at LIFAELS, La Salle, Universitat Ramon Llull, Barcelona, Spain.

^hAlso at Università di Bologna, Bologna, Italy.

ⁱAlso at Università di Roma Tor Vergata, Roma, Italy.

^jAlso at Università di Genova, Genova, Italy.

^kAlso at AGH - University of Science and Technology, Faculty of Computer Science, Electronics and Telecommunications, Kraków, Poland.

^lAlso at Universidade Federal do Triângulo Mineiro (UFTM), Uberaba-MG, Brazil.

^mAlso at Università di Cagliari, Cagliari, Italy.

ⁿAlso at Scuola Normale Superiore, Pisa, Italy.

^oAlso at Hanoi University of Science, Hanoi, Viet Nam.

^pAlso at Università di Bari, Bari, Italy.

^qAlso at Università degli Studi di Milano, Milano, Italy.

^rAlso at Università di Roma La Sapienza, Roma, Italy.

^sAlso at Università di Pisa, Pisa, Italy.

^tAlso at Università di Urbino, Urbino, Italy.

^uAlso at P.N. Lebedev Physical Institute, Russian Academy of Science (LPI RAS), Moscow, Russia.